Passive seismic experiment 'AniMaLS' in the Polish Sudetes (NE Variscides)

Monika Bociarska[1], Julia Rewers[1], Dariusz Wójcik[1], Weronika Materkowska[1], Piotr Środa[1] and *AniMaLS Working Group**

[1]Department of Seismic Lithospheric Research, Institute of Geophysics Polish Academy of Sciences, Warszawa, 01-452, Poland

*A full list of authors and their affiliations appears at the end of the paper.

Correspondence to: Monika Bociarska (bociarska@igf.edu.pl)

Abstract. The paper presents information about the seismic experiment AniMaLS which aims to provide a new insight into the crust~~al~~ and upper mantle structure beneath the Polish Sudetes (NE margin of the Variscan orogen). The seismic network~~array~~ composed of 23 temporary broadband stations was operat~~ing~~ed continuously for about two ~~2~~ years (October 2017 and October 2019). The dataset was complemented by records from 8 permanent stations located in the study area and in the vicinity. The stations were deployed with inter-station spacing of approximately 25-30 km. As a result, ~~good quality~~ recordings of local, regional and teleseismic events were obtained. We describe the aims and motivation of the project, the stations deployment procedure, as well as the characteristics of the temporary seismic network~~array~~ and of the permanent stations. Furthermore, this paper includes a description of important issues like: data transmission set-up, status monitoring systems, data quality control, near-surface geological structure beneath stations and related site effects etc. Special attention was paid to verification of correct orientation of the sensors. The obtained data set will be ~~modell~~analysed using several seismic interpretation methods, including analysis of seismic anisotropy parameters, with the objective of extending knowledge about the lithospheric and sub-lithospheric structure and the tectonic evolution of the study area.

1 Introduction

The passive seismic experiment AniMaLS (**Ani**sotropy of the **Ma**ntle beneath the **L**ower **S**ilesia) aims at studying the structure of the crust and upper mantle of the Polish Sudetes and Sudetic Foreland, as well as the processes of their orogenic evolution, using seismological and petrological methods. Up to now, the upper mantle in this region was only sparsely sampled by seismic data (Wilde-Piórko et al., 1999; Wilde-Piórko et al., 2008). A temporary seismic array deployed in the Polish Sudetes in a period from October 2017 to October 2019 collected ~~good quality seismic~~ broadband seismological data, which are an important prerequisite to image the lithospheric and sub-lithospheric properties of the Sudetes and the Lower Silesia. ~~region.~~

The main purpose of this paper is to present the research objectives of the AniMaLS project and technical information concerning the data acquisition. We describe the characteristics of the temporary seismic array and of the permanent stations in the study area. Also, we present details of the stations deployment procedure, including the site selection, sensor orientation, data transmission set-up, status monitoring systems. We also discuss near-surface geological settings of the sites and their relation with observed site effects. We describe the technical aspects of field measurements, distribution and acquisition parameters of the stations, and stages of data quality control. Attention was paid to the verification of the sensor orientation. Finally, we describe the data completeness, present data examples, and discuss the noise characteristics.

The Lower Silesian region comprises two major tectonic units: : the Sudetes mountains and the Sudetic Foreland, forming north-eastern part of the Bohemian Massif (BM) and representing NE termination of the Variscides Variscan internides in the Central Europe (Figures 1 and 2). Its present shape is a result of a long and complex tectonic evolution. The Variscan consolidation of this region involved accretion of several Proterozoic and Palaeozoic, mostly Gondwana derived terranes at the Laurussia margin. The lithosphere of this area was consolidated during the Variscan orogeny (Late Devonian to Early Carboniferous) as the result of multi-stage collision between paleocontinents of Laurussia and Gondwana and accretion of a group of smaller, Gondwana-derived, Proterozoic to Palaeozoic microplates (Armorican Terrane Assemblage, ATA) at the Laurussia margin (Franke et al., 2017). Accreted Neoproterozoic to Cambrian metamorphic blocks and nappe complexes, as well as early Palaeozoic volcano-sedimentary rocks, were intruded by several Carboniferous granitoid plutons. In some parts, the region of the Sudetes was covered by sedimentary sequences of Late Carboniferous syn- and postorogenic intramontane basins and Cretaceous to Cenozoic cover (Mazur et al., 2007).

At present, the lithosphere of the Sudetes is a mosaic of several units with distinct tectonic histories and with consolidation ages ranging from the upper Proterozoic to the Quaternary. The area is cut by three major right-lateral faults with WNW-ESE general orientation: Odra Fault Zone (OFZ), Sudetic Marginal Fault (SMF), and Intra-Sudetic Fault (ISF) (Aleksandrowski et al., 1997). The SMF divides the Sudetes block into the Sudetes mountains and Sudetic Foreland (Figure 2). The mountain ridge originated from the Cenozoic rejuvenation and differential uplift of an old Variscan area due to collision-related intraplate stress at the Alpine foreland during the last episode of formation of the Alps and Carpathians. As a result of the uplift, the Sudetes mountains are the most exposed fragment of the NE Variscan basement in Europe (Mazur et al., 2007). Present topography of Sudetes mountains is a result of Tertiary tectonic reactivation related to the Alpine orogeny.

Due to complex structure of the region, several controversies and open questions concerning its evolution are still present – e.g., on the validity of the strike-slip tectonics model vs. oroclinal bending model as general mechanism responsible for the present-day lithospheric structure (Mazur et al., 2020), as well as more detailed issues, concerning, for instance, the roles of the regional fault- and shear zones, the relationships between individual tectonic units and their ties with the structure and deformations of the underlying mantle. Therefore, presented project attempts to provide new data project aims for a deeper understanding ofon the structure, tectonic evolution and geodynamics of the NE Variscides with the use of using seismic

methods, based on recordings of local, regional and teleseismic events. The depth range of the experiment~~study~~ comprises

65 the crust and the mantle lithosphere, the lithosphere–asthenosphere boundary (LAB) and the sub-lithospheric upper mantle.
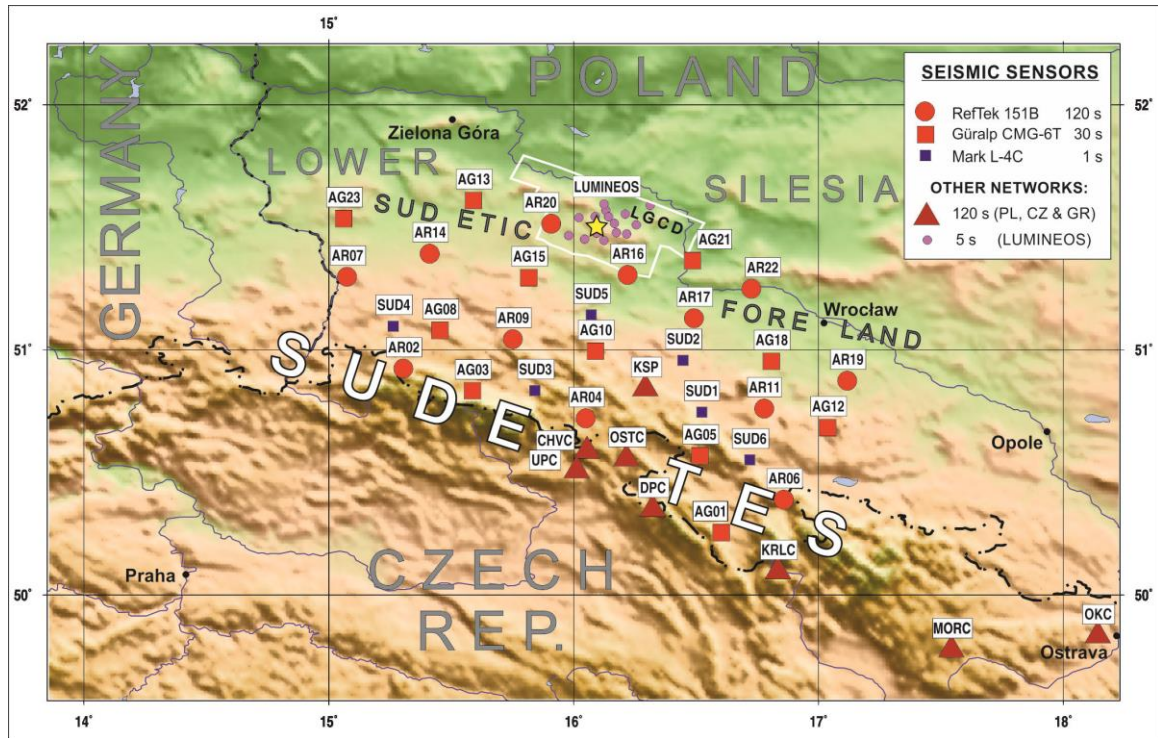
Figure 1: Location map of the AniMaLS experiment. The red circles are the temporary broadband sites with 120 s sensors, the red squares – temporary sites with 30 s sensors, the dark-red triangles are permanent stations (120s sensors). Blue squares – short-period (1 s) temporary stations. LGCD – Lubin-Glogów Copper District. Yellow star – epicenter of the local event discussed in
70 **Sect. 3. Elevation map based on GTOPO30 dataset (U.S. Geological Survey, 1996).**
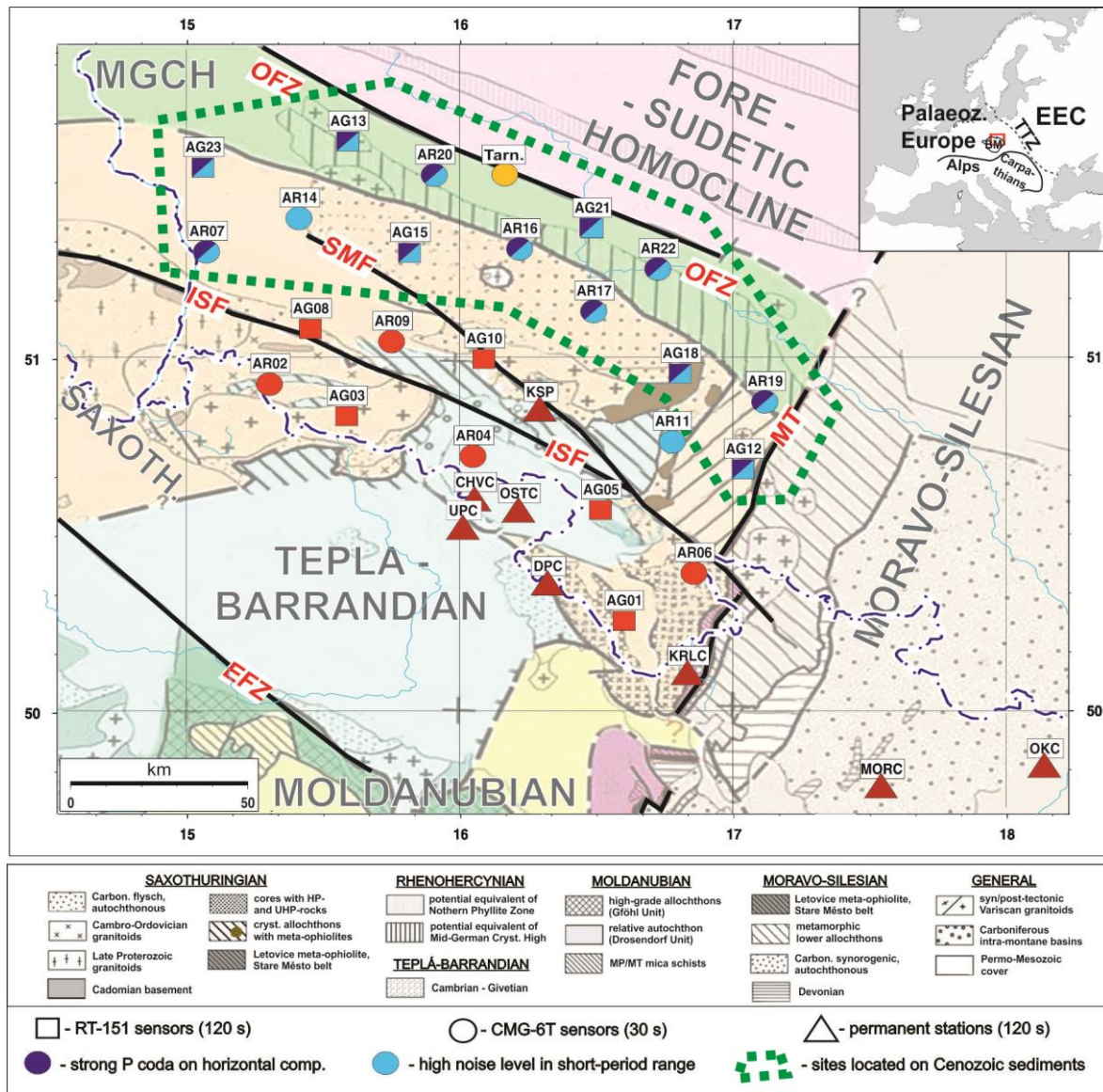
Figure 2̶1̶: Locations of temporary (circles and squares) and permanent (triangles) stations used in the experiment on a background of a tectonic map (modified after Franke et al., 2017). BM – Bohemian Massif, EEC – East European Craton, EFZ - Elbe Fault Zone, ISF - Intra-Sudetic Fault, MGCH – Mid-German Crystalline High, MT – Moldanubian Thrust, OFZ - Odra Fault Zone, SMF – Sudetic Marginal Fault, TTZ – Teisseyre-Tornquist Zone. Green dotted line delimits area where observation sites are located on C̶e̶ai̶nozoic sediments. Other stations are mostly located on Palaeozoic or Proterozoic basement, and two stations are on Cretaceous rocks. Light blue marks – stations with high noise amplitude in the short-period range, dark blue marks – stations showing high amplitude, long coda of the P-phase on horizontal components (see Sect. 3.1). Yellow circle - location of station in Tarnówek ̶i̶n̶ ̶L̶G̶C̶D̶ (Mendecki et al., 2016), discussed in Sect. 3.1.

Interpretation of the data with P- and S-receiver function will be attempted in order to trace the lithospheric and deeper (410 km and 660 km) discontinuities. ~~Moreover, t~~The project seeks to determine with more detail ~~the~~ seismic anisotropy ~~structure~~

of the mantle ~~and its seismic anisotropy, using~~with the use of the shear-wave splitting method applied to SKS and SKKS phases. The analysis of the P-wave polarization may also contribute to anisotropy studies. ~~Observations of the~~ Seismic anisotropy is closely related to mantle processes ~~of the seismic wave velocity are an important tool for studies of the processes shaping the lithosphere. The~~ its character ~~of the anisotropy~~ reflects the degree and the direction of tectonic deformations of the lithosphere (or the orientation of the sub-lithospheric mantle flow). ~~in the studied area. The analysis of the spatial distribution of seismic anisotropy will be attempted p~~ Potential spatial variations of ~~differences in~~ anisotropy parameters can be a proxy for discrimination between lithospheric blocks with different petrological composition or subject to different tectonic evolution. Obtained seismic results will be complemented with information from ongoing petrological studies of anisotropy of the mantle xenoliths in the Cenozoic volcanics, abundant in the Sudetes (Puziewicz et al., 2015) in order to get more constraints on the nature of the mantle anisotropy. Acquired recordings of local events may also be useful for other fields of seismological research, e.g., for studies of the local seismicity, seismotectonics and seismic hazard assessment.

Previous seismic research on the Polish Sudetes involved mainly studies of the crust and sub-Moho mantle with wide-angle reflection/refraction method (e.g., Majdański et al., 2006; Růžek et al., 2007; Grad et al., 2008) or, recently, with ambient noise tomography (Kvapil et al., 2021). The upper mantle in this area was studied with various methods by PASSEQ 2006-2008 experiment (e.g., Wilde-Piórko et al., 2008; Vecsey et al., 2014; Knapmeyer-Endrun et al., 2013). Numerous other seismic studies of the upper mantle, concentrating mainly on neighboring parts of the Bohemian Massif, are also closely related to the objective of the presented experiment (e.g., Babuška, 2008; Kind et al., 2017; Geissler et al., 2012; Karousová et al., 2012; Plomerová et al., 2012).

The main purpose of this paper is to present the research objectives of the AniMaLS project, technical information concerning the data acquisition and obtained dataset. In Sect. 2.1, we describe the characteristics of the temporary seismic network and of the permanent stations in the study area. Also, in Sects 2.2-2.5, we present details of the stations deployment procedure, including the site selection, sensor orientation, data transmission set-up and status monitoring systems. We describe the technical aspects of field measurements, distribution, acquisition parameters of the stations, and stages of data quality control. The near-surface geological setting of the sites is presented in Sect. 2.6. We describe data completeness and present data examples in Sect. 3. The noise characteristics, observed site effects and their relation to near-surface geology are discussed in Sect. 3.1. Finally, in Sect. 3.2, attention is paid to the data-based verification of the sensor orientation.

2 Station deployment

2.1 The network layout and equipment

The AniMaLS seismic network~~array~~ ~~has~~had been deployed between October 2017 and January 2018 and ~~it~~ was operated for a period of about two ~~2~~ years, until October 2019. Two institutions contributed to the temporary seismic network – the Institute of Geophysics, Polish Academy of Sciences (IG PAS) provided ~~with~~ 10 Güü~~u~~ralp CMG-6T ~~(equivalent of CMG-40T)~~ (30s corner period) seismometers with Güü~~u~~ralp DM24S3EAM data acquisition units and one CMG-6TD 30s seismometer and data acquisition unit~~recorder~~. The Institute of Geophysics of the University of Warsaw (IG UW) supplied 12 Reftek-130B data acquisition systems~~recorders~~ with broadband seismometers Reftek 151-120 "Observer" with bandwidth of 0.0083-50 Hz (120-0.02 s). Additionally, for observations of local seismicity, IG PAS deployed 6 units with short-period (1s corner period~~frequency~~) Mark L-4C sensors. All stations had 130 dB dynamic range and used 100 Hz sampling frequency. Timing was provided by GPS receivers. The average inter-station distance in the array was about 25-30 km.

As several permanent seismic stations were operated~~ing~~ in the study area, it was possible to enlarge the dataset with recordings of stations: KSP (Polish Seismological Network) and CHVC, DPC, KRLC, MORC, OKC, OSTC, and UPC (Czech Regional Seismic~~ological~~ Network), all equipped with 120 s sensors. The short-period (1s–5s sensors) LUMINEOS network, designed by IG PAS for monitoring of the induced seismicity in Legnica-Głogów Copper District (LGCD) (Mirek and Rudziński, 2017) is also in the area we are investigating. The distribution of the AniMaLS stations and permanent seismic stations used in the experiment is shown in detail in Figure 2~~1~~. The coordinates of the stations, locations names and technical details are summarized in Table 1.

Table 1. Location and technical parameters of the temporary and permanent stations used in the experiment, with lithology and stratigraphy information for observation sites.

Network	Station code	Operation period		Latitude [°]	Longitude [°]	Elev. [m]	Corner period [s]	Sample rate [Hz]	Sensor type	Site name	Lithology/stratigraphy at the surface
		From	To								
PD	AG01	21-10-2017	23-10-2019	50.2540	16.6020	477	30	100	CMG-6T	Ponikwa	limestones, marls (Upper Cretaceous)
PD	AG03	22-10-2017	23-10-2019	50.8329	15.5866	665	30	100	CMG-6T	Piechowice	granitoids (Upper Carboniferous)
PD	AG05	20-10-2017	22-10-2019	50.5675	16.5159	535	30	100	CMG-6T	Nowa Ruda	sandstones, mudstones (Carboniferous-Permian)
PD	AG08	23-10-2017	23-10-2019	51.0795	15.4545	387	30	100	CMG-6T	Rząsiny	phyllites, shales (Lower Palaeozoic)
PD	AG10	22-10-2017	23-10-2019	50.9946	16.0892	315	30	100	CMG-6T	Siedmica	greenstone shists, amphibolites (Lower Devonian)
PD	AG12	20-10-2017	22-10-2019	50.6827	17.0377	167	30	100	CMG-6T	Witostowice	Quaternary clastics on Lower Palaeozoic
PD	AG13	16-11-2017	24-10-2019	51.6099	15.5909	145	30	100	CMG-6T	Dzikowice	Quaternary clastics on Lower Palaeozoic
PD	AG15	23-10-2017	24-10-2019	51.2949	15.8169	152	30	100	CMG-6T	Groble	Quaternary clastics on Lower Palaeozoic
PD	AG18	19-10-2017	22-10-2019	50.9533	16.8070	121	30	100	CMG-6T	Kryształowice	Quaternary clastics on Lower Palaeozoic
PD	AG21	16-11-2017	25-10-2019	51.3643	16.4854	94	30	100	CMG-6T	Tarchalice	Quaternary clastics on Mesozoic
PD	AG23	13-04-2018	16-10-2019	51.5358	15.0611	145	30	100	CMG-6TD	Wymiarki	Quaternary clastics on Mesozoic
PD	AR02	29-12-2017	17-10-2019	50.9240	15.3048	550	120	100	RT151-120	Świeradów	schists, amphibolites

		Operation period		Latitude [°]	Longitude [°]	Elev. [m]	Corner period [s]	Sample rate [Hz]	Sensor type	Site name	Lithology/stratigraphy at the surface
										Zdrój	(Upper Proterozoic – Lower Palaeozoic)
PD	AR04	29-11-2017	17-10-2019	50.7202	16.0492	484	120	100	RT151-120	Lipienica	conglomerates, arkose sandstones, mudstones (Lower Permian)
PD	AR06	01-12-2017	18-10-2019	50.3894	16.8585	504	120	100	RT151-120	Orłowiec	schists, amphibolites (Upper Proterozoic – Lower Palaeozoic)
PD	AR07	07-05-2018	26-03-2019	51.2981	15.0742	177	120	100	RT151-120	Pieńsk	Quaternary clastics on Mesozoic
PD	AR09	29-11-2017	16-10-2019	51.0441	15.7518	342	120	100	RT151-120	Bełczyna	conglomerates, arkose sandstones, mudstones (Lower Permian)
PD	AR11	14-12-2017	18-10-2019	50.7605	16.7783	215	120	100	RT151-120	Ligota Wielka	gneisses, migmatites (Ordovician)
PD	AR14	17-11-2017	16-10-2019	51.3926	15.4122	145	120	100	RT151-120	Ławszowa	Quaternary clastics on Lower Palaeozoic
PD	AR16	01-12-2017	26-08-2019	51.3060	16.2202	129	120	100	RT151-120	Raszowa Mała	Quaternary clastics on Lower Palaeozoic
PD	AR17	14-11-2017	15-10-2019	51.1296	16.4912	141	120	100	RT151-120	Wrocisławice	Quaternary clastics on Lower Palaeozoic
PD	AR19	13-11-2017	18-10-2019	50.8739	17.1170	153	120	100	RT151-120	Kończyce	Quaternary clastics on Lower Palaeozoic
PD	AR20	15-11-2017	16-10-2019	51.5151	15.9078	135	120	100	RT151-120	Nowa Kuźnia	Quaternary clastics on Lower Palaeozoic
PD	AR22	13-12-2017	15-10-2019	51.2493	16.7257	17	120	100	RT151-120	Miękinia Głogi	Quaternary clastics on Lower Palaeozoic
PL	KSP	12-1999	present	50.8428	16.2931	353	120	20/100	STS-2	Książ	conglomerates, mudstones, limestones (Upper Devonian)
CZ	CHVC	05-2009	present	50.5881	16.0547	580	120	20/100	STS-2	Chvaleč	carbonatic sandstones, arkose sandstones (Lower Permian)
CZ	DPC	01-1993	present	50.3502	16.3222	748	120	20/100	STS-1	Dobruška/Polom	amphibolites, gabroamphibolites (Lower Palaeozoic)
CZ	KRLC	11-2008	present	50.0966	16.8341	614	120	20/100	CMG-3ESP	Králíky	gneisses (Lower Palaeozoic)
CZ	MORC	05-1994	present	49.7768	17.5425	742	120	20/80	STS-2	Moravský Beroun	shales, mudstones (Lower Carboniferous)
CZ	OKC	10-1998	present	49.8346	18.1399	250	120	20/100	CMG-3ESP	Ostrava/ Krásné Pole	shales, mudstones (Lower Carboniferous)
CZ	OSTC	10-2005	present	50.5565	16.2156	556	120	20/100	STS-2.5	Ostaš	marls, limestones (Upper Cretaceous)
CZ	UPC	05-2001	present	50.5074	16.0121	416	120	20/100	STS-2	Úpice	dolomitic sandstones, arkose sandstones (Upper Carboniferous-Permian)

135

Station Code	Operation period		Latitude [°]	Longitude [°]	Elev. [m]	Corner period [s]	Sample rate [Hz]	Sensor type	Site name	Lithology/stratigraphy at the surface
	From	To								
AG01	21-10-2017	23-10-2019	50.2540	16.6020	477	30	100	CMG-40T	Ponikwa	limestones, marls (Upper Cretaceous)
AG03	22-10-2017	23-10-2019	50.8329	15.5866	665	30	100	CMG-40T	Piechowice	granitoids (Upper Carboniferous)
AG05	20-10-2017	22-10-2019	50.5675	16.5159	535	30	100	CMG-40T	Nowa Ruda	sandstones, mudstones (Carboniferous-Permian)
AG08	23-10-2017	23-10-2019	51.0795	15.4545	387	30	100	CMG-40T	Rząsiny	phyllites, shales (Lower Palaeozoic)
AG10	22-10-2017	23-10-2019	50.9946	16.0892	315	30	100	CMG-40T	Siedmica	greenstone shists, amphibolites (Lower Devonian)
AG12	20-10-2017	22-10-2019	50.6827	17.0377	167	30	100	CMG-40T	Witostowice	Quaternary clastics on Lower Palaeozoic
AG13	16-11-2017	24-10-2019	51.6099	15.5909	145	30	100	CMG-40T	Dzikowice	Quaternary clastics on Lower Palaeozoic
AG15	23-10-2017	24-10-2019	51.2949	15.8169	152	30	100	CMG-40T	Groble	Quaternary clastics on Lower Palaeozoic
AG18	19-10-2017	22-10-2019	50.9533	16.8070	121	30	100	CMG-40T	Kryształowice	Quaternary clastics on Lower Palaeozoic

AG21	16-11-2017	25-10-2019	51.3643	16.4854	94	30	100	CMG-40T	Tarchalice	Quaternary clastics on Mesozoic
AG23	13-04-2018	16-10-2019	51.5358	15.0611	145	30	100	CMG-6TD	Wymiarki	Quaternary clastics on Mesozoic
AR02	29-12-2017	17-10-2019	50.9240	15.3048	550	120	100	RT_151-120	Świeradów Zdrój	schists, amphibolites (Upper Proterozoic – Lower Palaeozoic)
AR04	29-11-2017	17-10-2019	50.7202	16.0492	484	120	100	RT_151-120	Lipienica	conglomerates, arkose sandstones, mudstones (Lower Permian)
AR06	01-12-2017	18-10-2019	50.3894	16.8585	504	120	100	RT_151-120	Orłowiec	schists, amphibolites (Upper Proterozoic – Lower Palaeozoic)
AR07	07-05-2018	26-03-2019	51.2981	15.0742	177	120	100	RT_151-120	Pieńsk	Quaternary clastics on Mesozoic
AR09	29-11-2017	16-10-2019	51.0441	15.7518	342	120	100	RT_151-120	Bełczyna	conglomerates, arkose sandstones, mudstones (Lower Permian)
AR11	14-12-2017	18-10-2019	50.7605	16.7783	215	120	100	RT_151-120	Ligota Wielka	gneisses, migmatites (Ordovician)
AR14	17-11-2017	16-10-2019	51.3926	15.4122	145	120	100	RT_151-120	Ławszowa	Quaternary clastics on Lower Palaeozoic
AR16	01-12-2017	26-08-2019	51.3060	16.2202	129	120	100	RT_151-120	Raszowa Mała	Quaternary clastics on Lower Palaeozoic
AR17	14-11-2017	15-10-2019	51.1296	16.4912	141	120	100	RT_151-120	Wrocisławice	Quaternary clastics on Lower Palaeozoic
AR19	13-11-2017	18-10-2019	50.8739	17.1170	153	120	100	RT_151-120	Kończyce	Quaternary clastics on Lower Palaeozoic
AR20	15-11-2017	16-10-2019	51.5151	15.9078	135	120	100	RT_151-120	Nowa Kuźnia	Quaternary clastics on Lower Palaeozoic
AR22	13-12-2017	15-10-2019	51.2493	16.7257	17	120	100	RT_151-120	Miękinia Głogi	Quaternary clastics on Lower Palaeozoic
KSP	12-1999	present	50.8428	16.2931	353	120	20/100	STS-2	Książ	conglomerates, mudstones, limestones (Upper Devonian)
CHVC	05-2009	present	50.5881	16.0547	580	120	20/100	STS-2	Chvaleč	carbonatic sandstones, arkose sandstones (Lower Permian)
DPC	01-1993	present	50.3502	16.3222	748	120	20/100	STS-1	Dobruška/Polom	amphibolites, gabroamphibolites (Lower Palaeozoic)
KRLC	11-2008	present	50.0966	16.8341	614	120	20/100	CMG-3ESP	Králíky	gneisses (Lower Palaeozoic)
MORC	05-1994	present	49.7768	17.5425	742	120	20/80	STS-2	Moravský Beroun	shales, mudstones (Lower Carboniferous)
OKC	10-1998	present	49.8346	18.1399	250	120	20/100	CMG-3ESP	Ostrava/ Krásné Pole	shales, mudstones (Lower Carboniferous)
OSTC	10-2005	present	50.5565	16.2156	556	120	20/100	STS-2.5	Ostaš	marls, limestones (Upper Cretaceous)
UPC	05-2001	present	50.5074	16.0121	416	120	20/100	STS-2	Úpice	dolomitic sandstones, arkose sandstones (Upper Carboniferous-Permian)

2.2 Site selection and array design

Usually, Tthe sites for permanent broad-band seismic stations are usually carefully selected in areas with extremely low noise. The sensors are located in vaults designed to minimize noise resulting from thermal and atmospheric variations. Such a careful site preparation and installation is often not possible in case of temporary seismic projects, where selection of the location, installation and formal issues (permissions, rental contracts) have to be done in a short time and with limited resources. Additionally, to form a more or less uniform network, the sites should be located at similar inter-station distances, which is another constraint for the site location. When deploying the array, we attempted to obtain a compromise between several factors: low seismic noise, site availability, continuous power supply and good high signal level of the mobile telecommunications network (UMTS/LTE). signal. An important issue was high level of security, in order to avoid the damage or loss of the equipment. Meeting all these requirements was not straightforward, since in most of the locations the

level of anthropogenic noise was elevated due to high population density and industrial activities. In these areas, fulfilling both constraints (stations spacing and low noise) has been extremely hard. When possible, we placed the units at the unused basements of buildings, in the outbuildings or in rarely used public utility buildings. The sensors were placed on a hard surface – concrete or tiled floor, and in some cases a 5 cm thick granite slab was used for this.
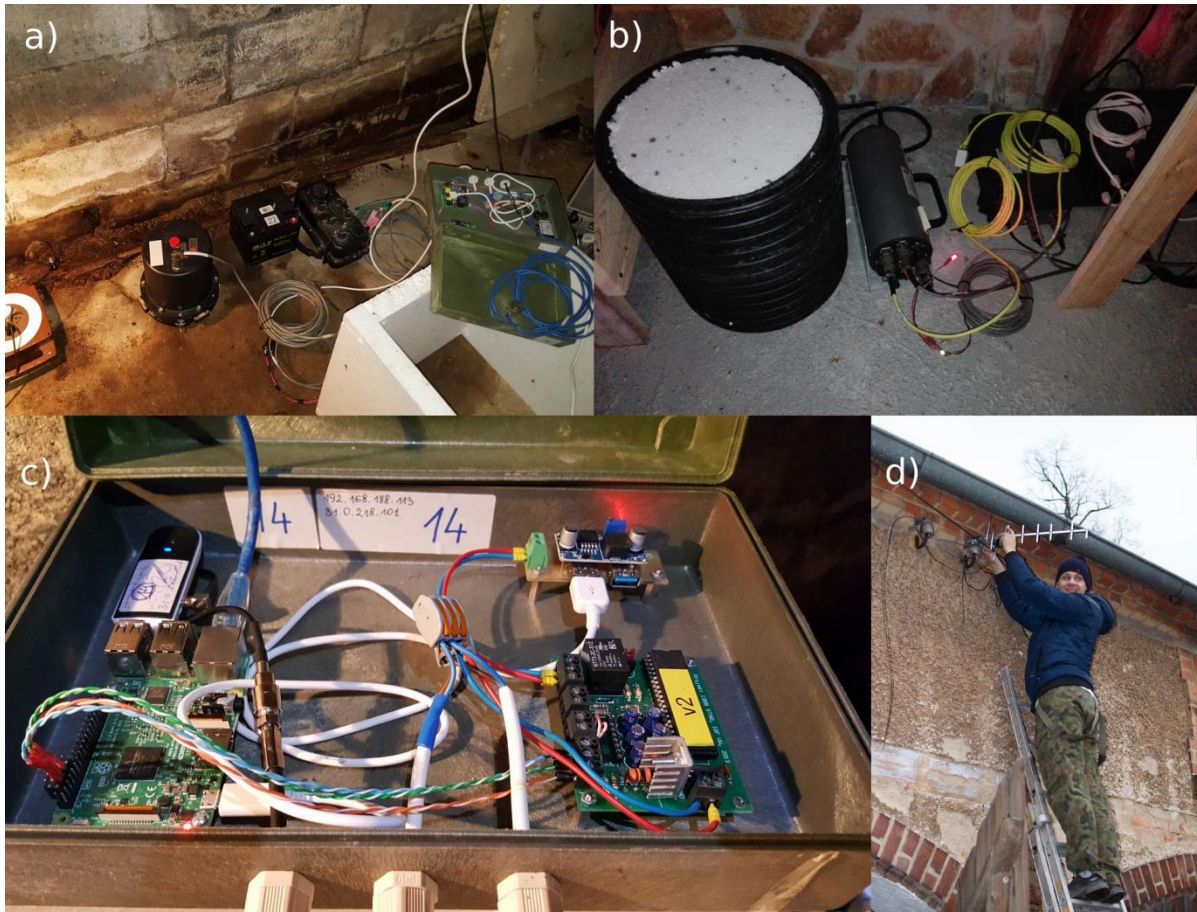
Figure 23: Deployment of seismic stations in the Sudetes: a) Reftek unit during installation, b) Installed Güüralp unit, c) data-transmission module – Raspberry Pi microcomputer with UMTS modem and watchdog, d) |Installing the UMTS antenna for data transmission.

At the sites, a thermal insulation of the sensor was ensured in a form of a stryrofoam box covering the sensor. A few pictures from installation of a typical station are shown in Fig. 32. Each station was powered by power grid system. The 12V power supply was buffered with 40-60 Ah batteries in order to ensure continuous operation of the units in case of the power outages. Near real-time data transfer was done with the use of UMTS/LTE mobile network connection.

2.3 Orientation of sensors

A precise orientation of seismic sensor axes with respect to geographical North direction is of great importance during installation of a 3-component seismic station. Incorrect orientation of the seismometer can result in substantial errors when using 3-component methods of interpretation, e.g., in case of shear wave splitting analysis (Ekström and Busby, 2008; Vecsey et al., 2014; Wang et al., 2016). The simplest method of geographical North determination, using a magnetic compass, often results in uncertainty exceeding 5° (Vecsey et al., 2017), which is not satisfactory for some interpretation methods. The modern approach, involving the use of an optical gyrocompass, allows for much higher precision, but requires expensive equipment.

Taking these limitations into account, we have designed our own low-cost system for precise orientation of the seismometers deployed in the project. For the determination of the geographical North direction in the field, we used a global navigation satellite systems (GNSS) unit with real-time kinematic positioning (RTK) technology unit and ASG-EUPOS network (Ryczywolski et al., 2008) for receiving location corrections. Two ways for transferring the North direction to the seismometer location was considered. First method was geodetic tachymetry. However, this method is not only time-consuming but also causes problems in less accessible locations such as basements. To solve this problem, we developed a simple device for azimuth transfer which makes the process more time-efficient while retaining satisfactory precision.

The core of the device is a MEMS triple axis accelerometer and gyroscope unit MPU-6050, controlled by a single-board Raspberry Pi microcomputer. The data communication between device modules is based on I2C serial protocol over the General Purpose Input Output (GPIO) ports. The code for processing the data from the gyroscope unit was written as a Python script. Raw data from the unit are converted into stable values of the rotation angle of the device. Problem of the gyroscope drift was solved by calibration of the immobile device prior to the measurement phase. During calibration the drift is evaluated, and, based on this, corrections for drift are continuously applied during the measurement.

Orienting the seismometer towards the geographic North with this method is done in two stages. First, GNSS RTK unit is used to obtain precise positions of two points of a baseline outside of the station site and to calculate the azimuth of the baseline as a reference. Next, the azimuth is transferred to the place where the seismometer will be installed. To this end, the gyroscope device is aligned parallel to the baseline using laser pointer, and GNSS-measured reference azimuth value is input to the device. The device is then moved indoor to the station site where it is rotated to North, according to displayed current azimuth, and the N-S line is marked on the floor at the location of the sensor. Finally, to check if the device readings were stable during the North measurement at the site, the device is moved back to the baseline and oriented along it, where, ideally, reference azimuth value should be again displayed. If the value differs substantially from the reference, it indicates excessive/variable drift or other errors, and the measurement is considered to be invalid. The procedure is repeated until 2-3 stable (negligible drift) and consistent measurements are obtained. Assuming availability of the GNSS RTK unit, this method is an affordable solution which allows for orientation of the sensor with error determined in field tests to be at the

level of ±2 degrees. order. Additionally, a data-based verification of the orientations was done with use of polarization analysis. The results are discussed in Sect. 3.2.

2.4 Real-time data transmission and data storage

The seismic data were written in the internal storage of the data acquisition units recorders (Güuralps - 16GB Flash memory, Refteks 2x16GB CF cards) and, simultaneously, they were transmitted in near real-time to dedicated acquisition servers at the IG PAS. Additionally, state of health (SOH) information including temperature, voltage, and mass positions were transmitted. The data transmission was done using UMTS internet connection, with all devices running IPsSec VPN system to securely connect all the stations to the data acquisition server and to protect the system from unauthorized access. The Güuralp units were connected to the network using Mikrotik routers with LTE modems. The data transfer to a dedicated CMG-NAM data hub was based on GDI protocol with a back-fill buffer, which allows for handling temporary loss of internet connection and retransmission of missing data packets after the connection is re-established. Connection loss and router/modem hang-up situations were handled by data acquisitionrecorder unit by an implemented software watchdog, which allowed for three3 levels of action: (1) soft reset of the modem, (2) power-cycling of the modem, and (3) power-cycling of the unit and of the modem. For data transmission from Reftek units, a modified system designed at IG UW (Polkowski, 2016), based on Raspberry Pi Linux microcomputers with UMTS or /LTE wireless modems was used. The Raspberry Pi units served both as routers and as devices scheduling the data transmission - collecting data from acquisition units recorders and sending them to server (FTP, rsync and SSH protocols). The control scripts (PHP, bash) were designed to check for gaps in transferred data (due to e.g., network connection loss, server or device hang-up) and to schedule data retransmission, if necessary. Hardware watchdog devices, designed at IG UW (Polkowski, 2016), were used to assure automatic restart of the transmitting unit on no connection or hang-up.

Both Güuralp and Reftek stations were remotely controlled and monitored using their proprietary software providing a WWW control interface. It allowed for checking the status of the individual units, mass positions, timing, voltages, temperature, as well as setting various recording parameters. For Reftek units, the control interface alllowed for monitoring of mass positions and mass centering. Also, automatic mass centering could be triggered if mass voltages exceeded a threshold after a user-defined time.

The near real-time data transfer has well-known advantages - inspection of the current data flow and access to current SOH information is useful for monitoring of the data quality and allows for fast detection of failures, such as power supply malfunctions or timing problems. Also, an increase of the noise level or the signal distortion due to an inadvertent moving or tilting of the sensor can be detected, and necessary station maintenance can be planned. This saves the number of the field trips needed for servicing the stations and helps to quickly reestablish proper acquisition of the seismic data.

The gaps in transmitted data resulting from the lack of UMTSGSM connection were filled by periodic retrieving of the recorded data directly from the data acquisition system recorder memory during stations maintenance in the field, if needed.

The transmitted and patched data were stored in miniSEED format. After unification of information in headers, the daily
miniSEED files were finally stored in the form of SeisComP Data Structure (SDS) – a hierarchical structure with file and
directory naming convention which allows for easy access to the data, e.g., with the ObsPy package.

2.5 Station timing

The seismic studies require exact measurement of absolute time of the seismogram to be able to determine the arrival times
of the analysed phases. An incorrect timing may lead to erroneous identification of the phases or incorrect travel-time
determination. Currently, the seismic acquisition systemsrecorders use GPS/GNSS receivers that allow for the
synchronization of the internal clock with a high accuracy (±10 μs). However, in practice, technical malfunctions or loss of
GNSS signal can introduce timing errors, and such problems should be recognized. If possible, incorrect timing should be
corrected during initial data processing, or reported, to avoid using badly timed data for the interpretation. During the data
acquisition for the project, an important problem with timing occurred for five5 Reftek acquisition unitsrecorders due to the
"Week Number Roll-Over" (WNRO) issue in the GPS system in 2019, which affected the GPS receivers with older
hardware, not designed to cope with this issue. As a result, in July 2019, some of the stations started to report the date with
wrong year (e.g., 2099) and incorrect day of year. However, the correct time of the day was preserved, therefore it was easy
to obtain proper date by shifting the time by a fixed amount of full days. Corrected date/time was then written into
miniSEED headers. Nevertheless, the wrong date caused malfunction of the online data transmission system, which expected
a correct date in the transmitted file names and in the headers. The transmission system software had to be temporarily
modified in order to avoid the problem. Permanent solution of the problem was later achieved by updating recorders'
firmware with patched, WNRO-aware version.

Other problem was detected at the AG23 station, equipped with CMG-6TD dataloggerrecorder: after few weeks, the internal
clock lost synchronization with GPS time, in spite of properly working and locked GPS receiver. This resulted in a linear
increase of the time difference, which reached ~20 s after few months of recording. In this case, only an approximate time
correction was possible. By comparing the timing of good-quality arrivals in seismograms from AG23 and neighboring,
correctly timed stations, it was possible to measure the time differences over the recording period, and to apply appropriate
corrections. Here, the accuracy of time determination after the correction was estimated to ~1 s. This is a relatively large
value, and it prevents such data from being used for modelling methods which require exact knowledge of the absolute time,
as e.g., seismic tomography. Nevertheless, such data can still be used in methods based on relative time of the seismogram
components, as receiver function method or shear-wave splitting. More precise determination of timing corrections for this
station is planned with the use of a method based on the noise correlation between recordings from incorrectly timed station
and neighboring, correctly timed ones (Sens-Schönfelder, 2008).

2.6 Characteristics of observation sites and near-surface geology

255 The geology of the near-surface sequences varies considerably over the study area, ranging from Proterozoic crystalline rocks to unconsolidated Quaternary sequences. The geological structure of the basement at the observation site can heavily affect the character of the recorded seismograms, therefore we summarize the differences in the near-surface lithology and discuss their possible influence on the seismic data. The Table 1 presents locations, technical information (sensor type, operation time), lithology and stratigraphy at the site for temporary and permanent stations. Geological information is based
260 on the Geological Map of Poland 1:500000 (Państwowy Instytut Geologiczny - Państwowy Instytut Badawczy, 2021), and Geological Map of Czech Republic 1:50000 (Geological map 1~~:~~50000, 2021).

In the SW part of the study area (roughly corresponding to the Sudetes mountains), the observation sites are located directly on consolidated rocks of Palaeozoic or Proterozoic basement (except AG01 and OSTC, positioned on Cretaceous rocks). The stations in the NE (the less-elevated region of Sudetic Foreland) are located on a layer of ~~Quaternary and Tertiary~~Cenozoic
265 unconsolidated sediments, overlying the Palaeozoic basement. This area is marked in Fig. 3 with a green dotted line. The presence of the low-velocity C~~ai~~enozoic deposits at these sites has a distinct influence on the seismic records, and more detailed discussion of these effects is presented in Sect. 3.1.

270 **3 Data**

Figure 4 presents the epicenters of the earthquakes with magnitude above 5.5 which occurred during the registration period (October 2017 – October 2019), a~~A~~ccording to the International Seismological Centre (ISC) catalogue (1285 events). ~~, during the registration period (October 2017 – October 2019) 1285 events with magnitude above 5.5 occurred. These earthquakes are shown in Fig. 4. Size of the dots represents the event magnitude.~~ Figure 5 shows the data availability
275 diagram for the stations of the network~~array~~, produced using ObsPy package (Krischer et al., 2015~~Beyreuther et al., 2010~~). Several shorter gaps, mostly resulting from data transmission problems and some longer gaps (caused by hardware failures or power shortages due to heavy thunderstorms) are present. The overall completeness of the network-transmitted data, supplemented with untransmitted data after recovery in the field, is 97%.
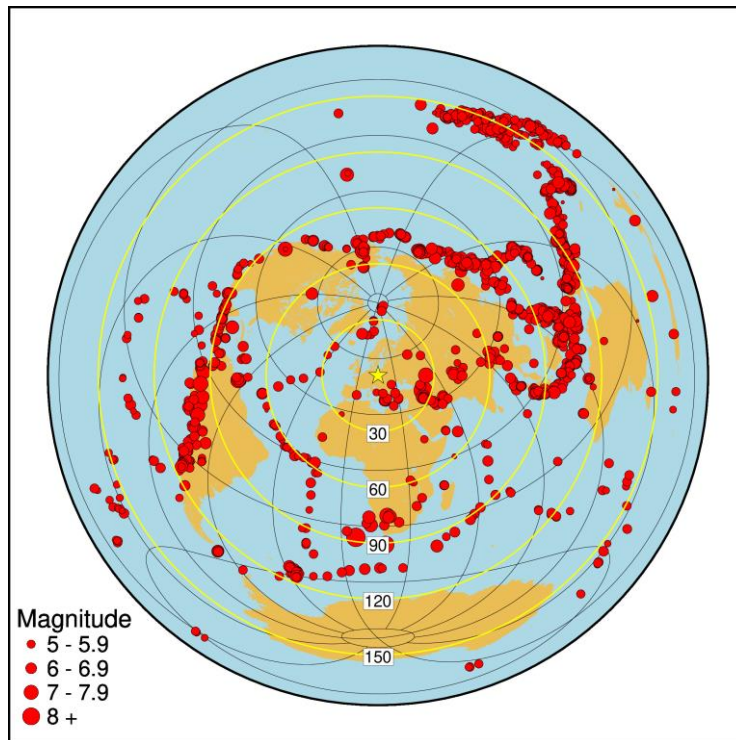
280 **Figure 4: Distribution of the epicenters of M > 5.5 earthquakes in the period from 18 Oct 2017 to 26 Oct 2019, according to ISC catalogue (1285 events). The yellow asterisk represents the center of the AniMaLS seismic array in the Sudetes. The yellow circles mark the distances (in degrees) from the array center in 30° steps.**
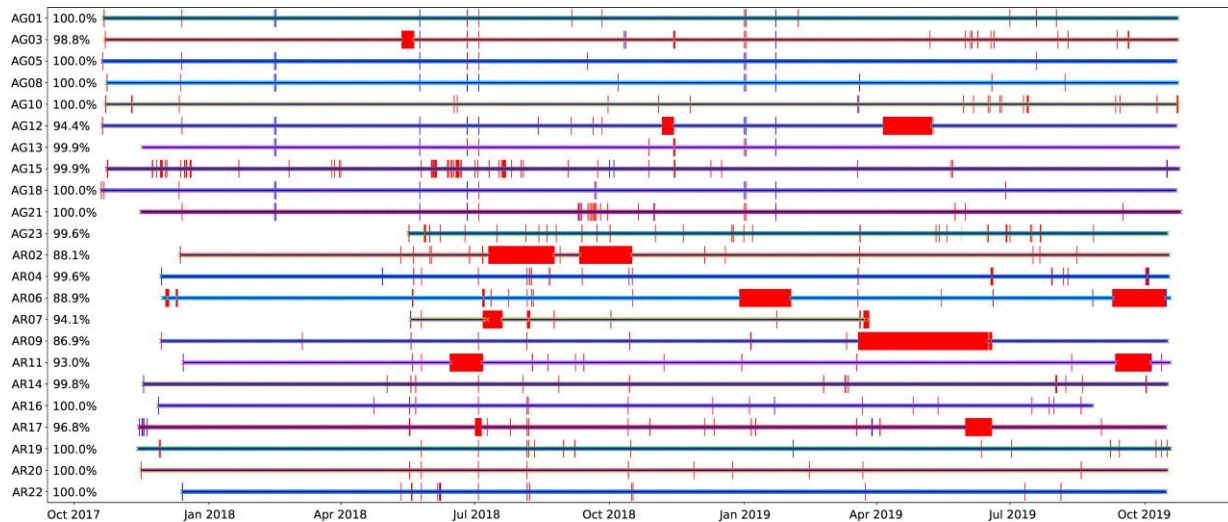
Figure 5: The diagram showing the data completeness for temporary stations. Red fragments – gaps in the data resulting from stations failures, memory cards errors and power shortages.
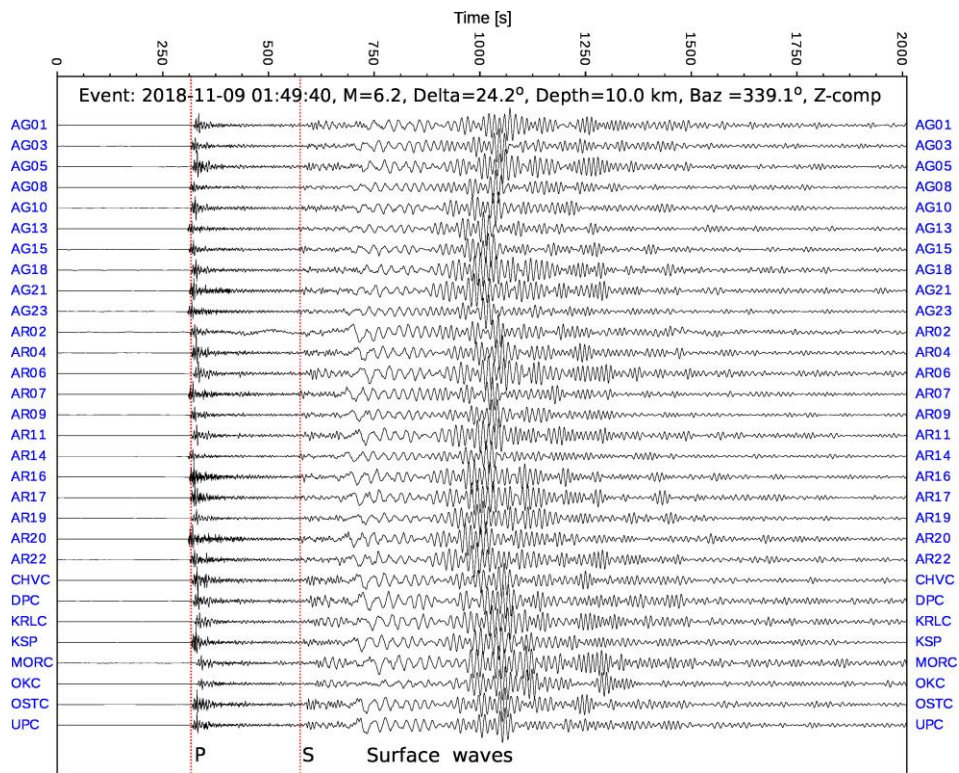
285 **Figure 6: Example of vertical component of recorded waveforms for the M6.2 teleseismic earthquake which occurred 2018-11-09 in Jan Mayen Island region (lat: 71.6312, lon: -11.2431, depth: 10.0 km after ISC). Red lines mark the theoretical onsets of P- and S-phases at the KSP station. All seismograms are low-pass filtered ($<$ 1 Hz).**
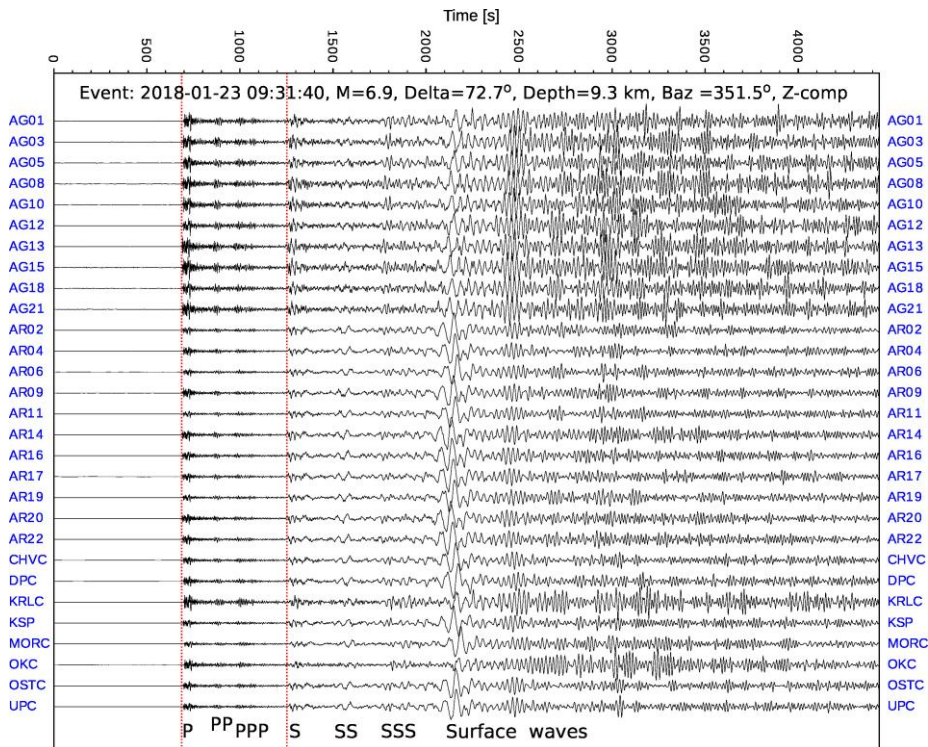
Figure 7: Example of vertical component of waveforms recorded for the M6.9 teleseismic earthquake which occurred 2018-01-23 near Alaska (lat: 55.9315, lon: -149.1877, depth: 9.3 km after ISC). Red lines mark the theoretical onsets of P- and S-phases at the KSP station. All seismograms are low-pass filtered (< 1 Hz).

Figure 6 presents an example of seismograms for an earthquake near Jan Mayen Island. ~~with M = 6.2, at epicentral distance Δ = 24°. It occurred 2018-11-09, 01:49:40.05 UTC (lat: 71.6312, lon: -11.2431, depth: 10.0 km after ISC). The red dotted lines mark the theoretical arrival times of P- and S-waves at the KSP station.~~ The seismograms show strong P-wave arrivals and lower-amplitude S arrivals, followed by high-amplitude surface (LR) waves, showing distinct dispersion. Figure 7 shows an example of a teleseismic earthquake from Alaska area. ~~(M = 6.9, Δ = 73°), which occurred 2018-01-23, 09:31:40.91 UTC (lat: 55.9315, lon: -149.1877, depth: 9.3 km after ISC).~~ Here, besides high-amplitude P- and S-waves, also free-surface reflections PP, PPP, SS, and SSS can be clearly observed. Starting from ~2050 s relative time, a long train of surface waves with substantial dispersion is visible. ~~Interestingly, t~~This figure clearly shows differences in frequency response of sensors for two groups of stations (it should be noted that records are scaled to maximum amplitude of each seismogram). For the AR- and permanent stations, equipped with 120 s sensors, the strongest amplitude is seen for the earliest, long-period (~50 s) pulses of surface wave at ~2050-2150 s time. However, for AG- stations, these long-period pulses are outside the 30 s corner frequency of the sensors and are strongly attenuated. With maximum trace amplitude scaling applied, this leads to substantial enhancement of amplitudes of remaining parts of the seismogram: the body-wave pulses and later surface wave trains (with periods < ~30 s) for AG- stations, relative to AR- and permanent stations records.
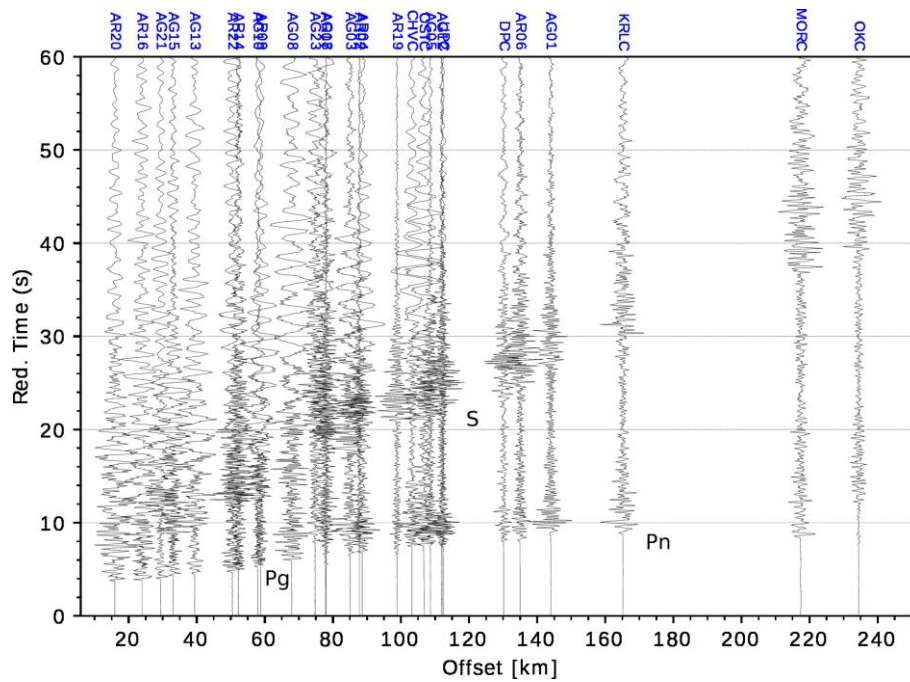
Figure 8. Example of waveforms recorded for the M4.4 local earthquake which occurred 2018-07-03, 19:38:47.75 UTC in Legnica-Glogów Copper District (lat: 51.5145, lon: 16.1378, depth: 0.0 km after ISC). Band-pass filter 0.2-15 Hz was used. Reduction velocity is 8 km/s. Location of the epicenter is shown in Figure 2.
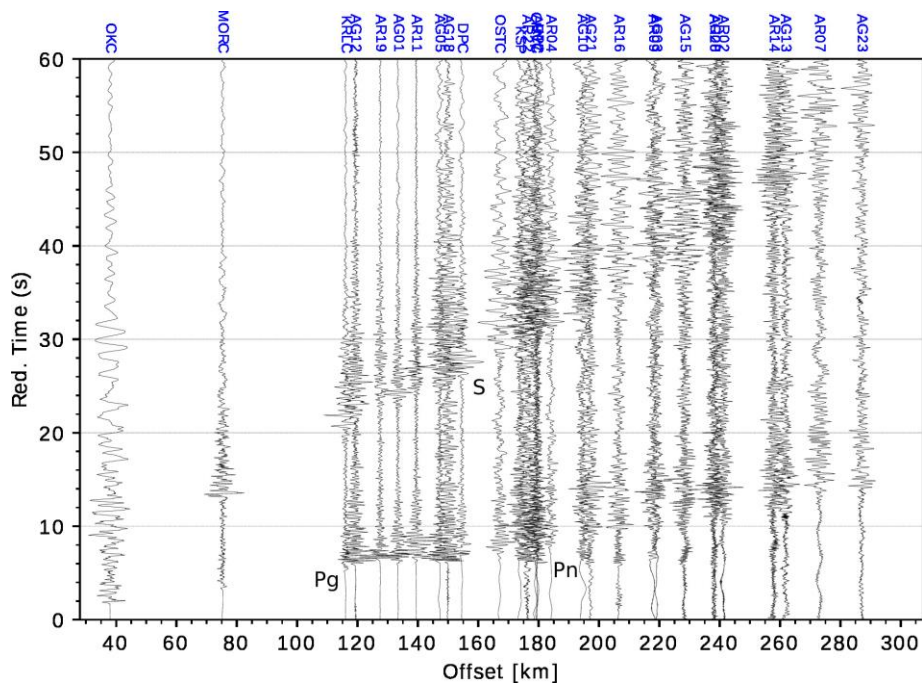
310 **Figure 9: Example of waveforms recorded for the M3.9 local earthquake which occurred 2019-01-22, 22:35:30.08 UTC in Upper Silesia district (lat: 50.1095, lon: 18.4559, depth: 5.5 km after ISC). Band-pass filter 0.2-15 Hz was used. Reduction velocity is 8 km/s.**

Figures 8 and 9 show local earthquakes from Legnica-Głogów Copper District and from Upper Silesia district, respectively.

Both events are related to local mining activities. ~~The first event with magnitude 4.4 occurred 2018-07-03, 19:38:47.75 UTC~~

315 ~~(lat: 51.5145, lon: 16.1378, depth: 0.0 km after ISC), the second one, with magnitude 3.9, occurred 2019-01-22, 22:35:30.08~~

~~UTC (lat: 50.1095, lon: 18.4559, depth: 5.5 km after ISC).~~ These figures show the Z-component with 0.2-15 Hz bandpass

filter. The epicentral distances are in the range of 0-240 km for Legnica-Głogów event and 40-300 km for Upper Silesia

event. At these distances, we observe strong crustal phases ~~strong~~ (Pg) ~~phase~~, and mantle refraction (~~the~~ Pn phase) in the

first arrivals. The Pn appears at offsets > ~140 km. At larger times, strong S-waves and surface waves are recorded.

320
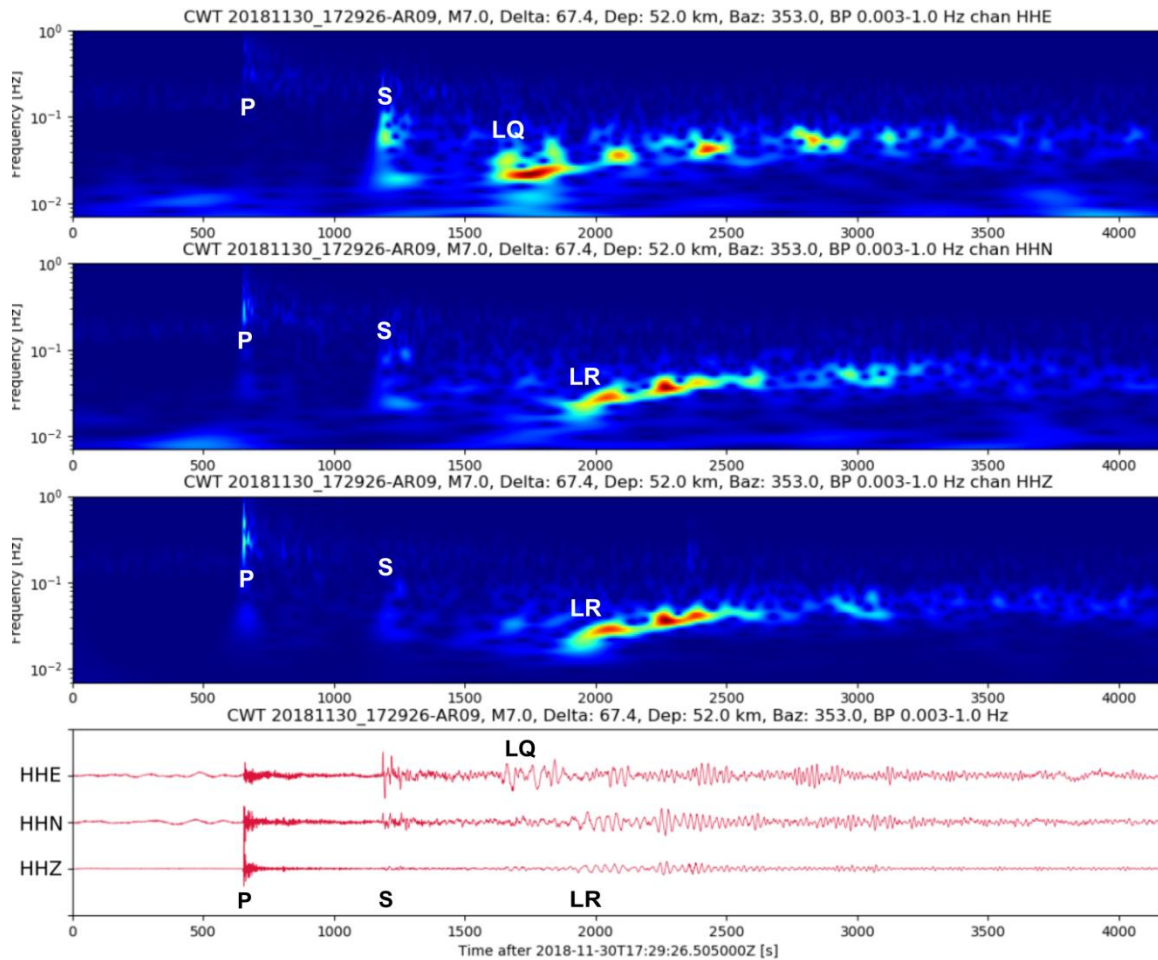
Figure 10: Spectral seismograms obtained with the use of~~using~~ ~~C~~continuous ~~W~~wavelet ~~T~~transform for station AR09, showing a teleseismic event from Southern Alaska, 2018-11-30, 17:29:26 UTC. From top to bottom: E-, N- and Z-component.

An example of time-frequency representation of the data is shown in Fig. 10. Here, a spectral seismogram obtained with the

325 use of~~using~~ continuous wavelet transform (Daubechies, 1992) is presented for a teleseismic event (Southern Alaska, epicentral distance 67°, backazimuth 353°) recorded by AR09 station. The Morlet wavelet was used. The onset of the P-wave is visible at ~600 s relative time, in records of Z- and N-component, with maximum amplitude in 2-4 s period range. At ~1200 s travel time, the S-waves with periods in 12-15 s range are visible, with the largest amplitude on E- component. The body waves are much weaker than surface waves, which are visible at larger travel times. On the E-component,

330 corresponding approximately to transverse direction relative to ray backazimuth, the LQ waves with a period of 50-60 s can be seen at ~1600 s time. The LR waves, best visible on N- and Z-component records at ~1900 s, clearly show the dispersion, with period decreasing~~changing~~ from 40 s to 25 s.

3.1 Seismic noise characteristics and site effect

To estimate the level of the ambient noise at various frequencies, we calculated the probabilistic power spectral density (PPSD) distributions (McNamara and Buland, 2004) for the data recorded at each station with the use of ~~using~~ ObsPy package (Krischer et al., 2015~~Beyreuther et al., 2010~~). The PPSDs was calculated for~~using~~ continuous recordings from the period 01.12.2018-01.10.2019 (22 months).

The PPSD calculation was based on analysis of 1-hour-long windows of continuous seismic data (with 0.5 h overlap). The processing sequence consisted of demeaning, tapering, FFT computation and instrument response removal. The obtained frequency spectra for all windows were smoothed and summed to form a histogram representing the frequency distribution of noise amplitudes at various period ranges. The result shows which amplitudes are observed for a given period. The PPSD medians were also calculated.

Figure 11 shows a comparison of the PPSDs for three types of stations: AG10 (with 30s CMG-6T~~40T~~ sensor), AR06 (RT 151-120s sensor) and permanent station UPC (STS-2 sensor). Diagrams for three components are presented. Figure 12 shows the PPSDs of Z-component for 12 selected temporary and permanent stations used in this study (PPSDs for all stations are presented in supplement Figure S1). Figure 13 shows a comparison of PPSD median curves for all sites used, including permanent and temporary stations. There is a systematic difference in the noise level between permanent and temporary sites. The difference is notable for long-period range (> 10 s), and is particularly large for the horizontal components. High amplitude of the noise for the long periods of the horizontal components is often experienced in case of temporary stations, mainly due to an imperfect protection from environmental thermal/pressure changes or the sensor base tilt (Wilson et al., 2002). Another factor contributing to higher long-period amplitudes on the horizontal component with respect to vertical amplitudes, in particular for stations located on young/low velocity sediments, could be the ellipticity of the Rayleigh waves. In presence of a low-velocity layer, the Rayleigh waves exhibit horizontally flattened particle motion, whereas at hard-rock sites on consolidated/crystalline basement, the particle motion is vertically elongated (Tanimoto et al., 2013). However, here, this factor seems to have a minor influence, considering relatively small (< 1 km) thickness of the low-velocity layer in this area, which should not affect the ellipticity of long-period (> 10 s) waves in question.
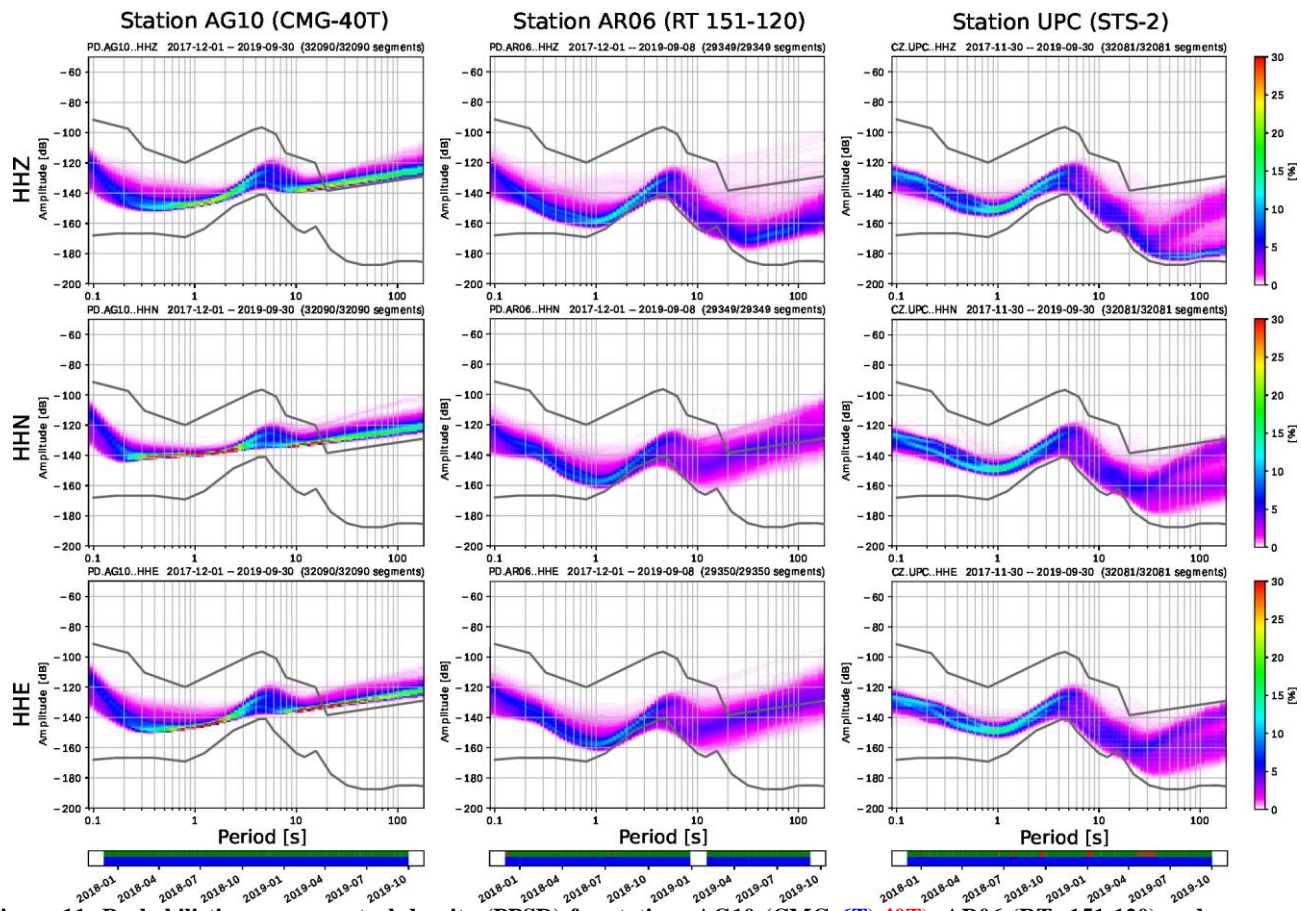
Figure 11: Probabilistic power spectral density (PPSD) for stations AG10 (CMG-6T).40T), AR06 (RT- 151-120) and permanent station UPC (STS-2). The Z, N and E components at the top, middle and bottom, respectively. The time span for calculation is 22 months from Jan 2018 to Oct 2019. Black lines mark New High and Low Noise Models (NHNM, NLNM; Peterson 1993).
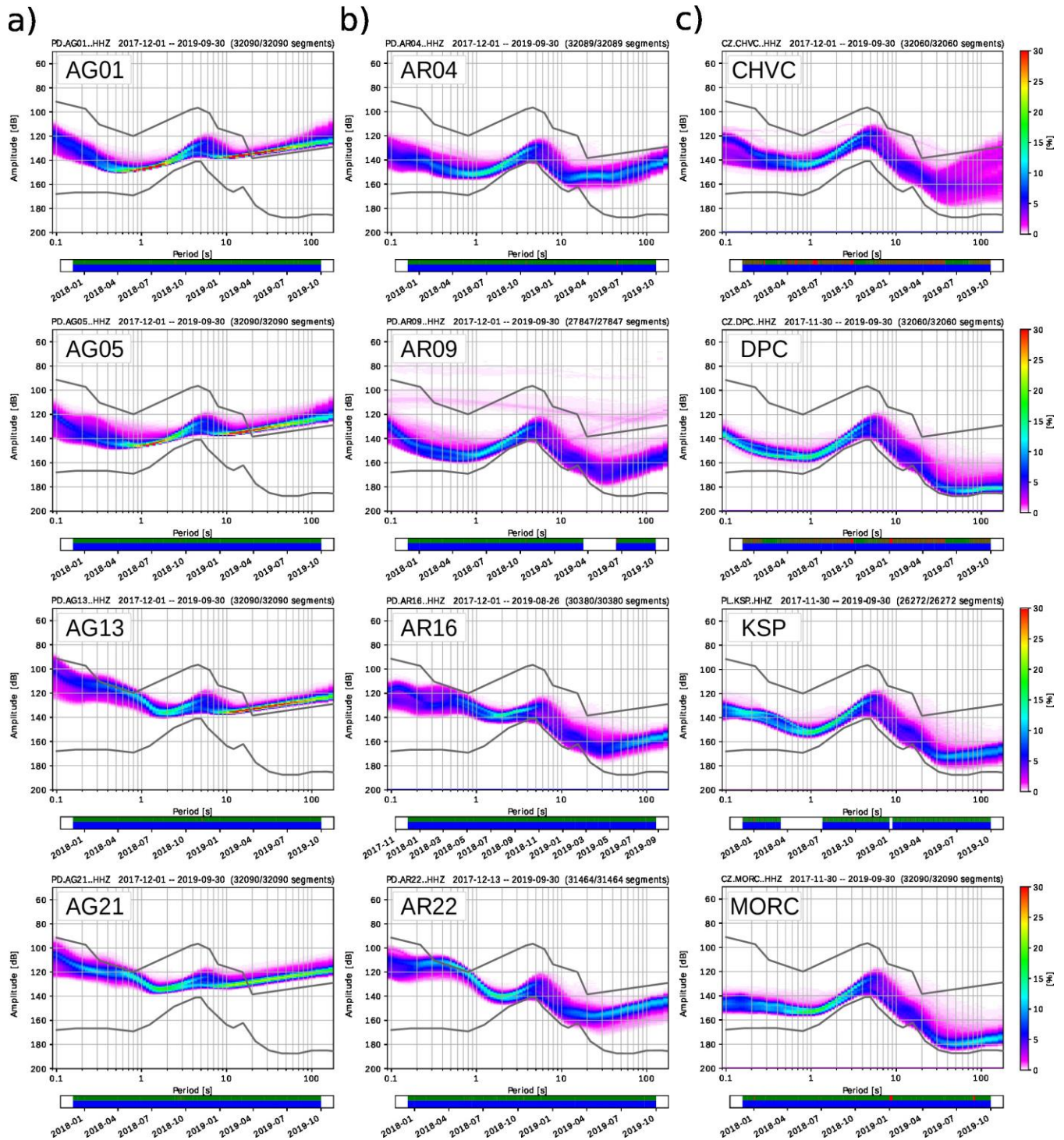
Figure 12: Probabilistic power spectral density (PPSD) on the Z-component for 12 selected stations. a) CMG-6T sensors, b) RT 151-120 sensors, c) permanent stations. Black lines mark New High and Low Noise Models (NHNM, NLNM; Peterson 1993).

360

The highest amplitude of the long-period noise, often exceeding New High Noise Model (NHNM) level, characterizes all sites with 30 s CMG-6T~~40T~~ sensors. ~~Previous studies show s~~Similar behaviour of these sensors, independently of the actual noise at the site was reported by Tillmann (2006). ~~(Evangelidis and Melis, 2012; Custodio et al., 2014, Staehler et al., 2016).~~ This is most likely due to high self-noise of this device type, and, partially (for $T_{noise} > 30$ s), to lower corner period of the instrument~~CMG 40T device~~ (30 s vs. 120 s for other units). It is worth noting that the CMG-6T high long-period noise is at the very similar level as for the OBS version of the Güralp CMG-40T (30 s) sensor (Stähler et al,. 2018), while the land version of CMG-40T shows substantially lower (by about 20 dB) self-noise in this period range (Custodio et al., 2014; Tasič and Runovc, 2012).
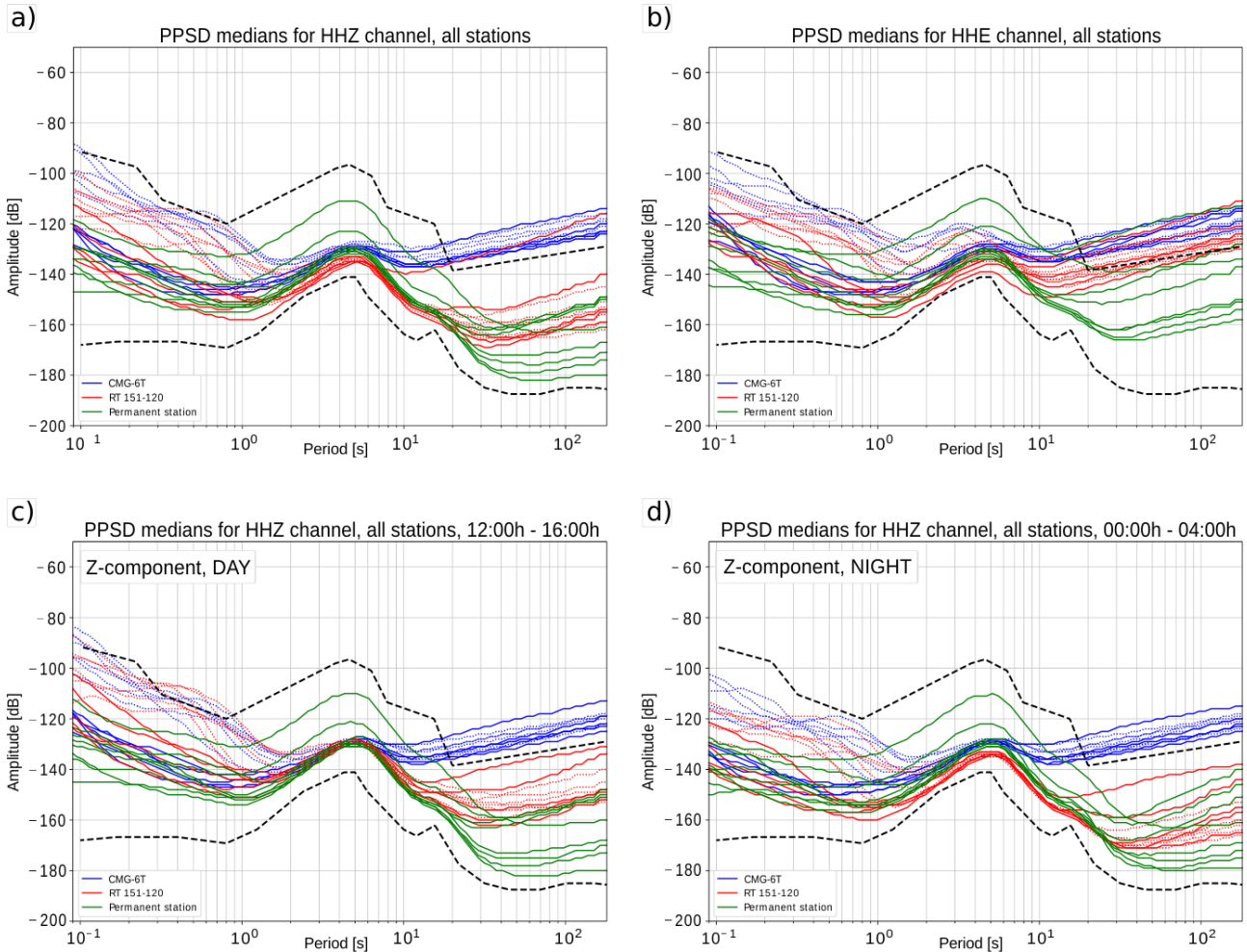
Figure 13: The PPSD median curves for all temporary and permanent stations. a) Z-component, b) E-component, c) Z-component, day~~night~~ hours only (12~~00~~:00-16~~04~~:00 local time), d) Z-component, night hours only (00:00-04:00 local time). Dotted lines – stations located on Quaternary sediments, solid lines - stations located on Palaeozoic or older basement. Time span for calculation is 22 months from Jan 2018 to Oct 2019. Black lines mark New High and Low Noise Models (NHNM, NLNM; Peterson 1993).

The short-period (SP) parts of the all PPSD medians (Fig. 13) show amplitude differences independent of the station type, and can be subdivided into two groups. Stations located on Palaeozoic, or older, consolidated basement (solid lines in Fig. 13~~2~~) show much lower noise in this part of the spectrum than the stations on the basement covered by unconsolidated, allu-

380 vial Cenozoic ~~Quaternary/Tertiary~~ sequences (dotted lines). This area represents NE part of the network~~array~~, marked with green dotted line in Fig. 3. The stations with high amplitude of the short-period noise, marked with light blue color, mostly fit into this region, which suggests a high correlation of this effect with the basement type. When attempting to interpret these differences in terms of the near-surface geology, care must be taken, because the high-noise sites installed on the Quaternary cover are, in the same time, located in the area with higher population density, denser network of roads, expressways

385 and railroads, with typically higher anthropogenic noise. To check if~~eliminate or minimize the influence of~~ the anthropogenic~~cultural~~ effects are responsible for these differences in short-period noise level, two variants of the PPSD medians were calculated ~~also~~ for the same time span~~n (22 months)~~: ~~but~~ only for day~~night~~ hours – from 12~~00~~:00h to 16~~04~~:00h local time, every day~~and only for night hours – from 00:00h to 04:00h local time~~. Comparison of results (Fig. 13c,d) shows that the SP noise level during day generally exceeds the night noise by 5-15 dB for all stations, irrespectively of their location. ~~The~~

390 ~~result (Fig. 13c) still shows clear~~ In the same time, difference~~s~~ in the short-period noise level~~amplituse~~ between the sites located on old Palaeozoic rocks and the sites on the young Quaternary cover are of similar amplitude (~ 25 dB) for day- and night-time PPSDs, suggesting that they are indeed related to the basement type at the sites.

Event: 2018-11-30 17:29:26, M=7.0, Delta=67.4°, Depth=52.0 km, Baz=353°
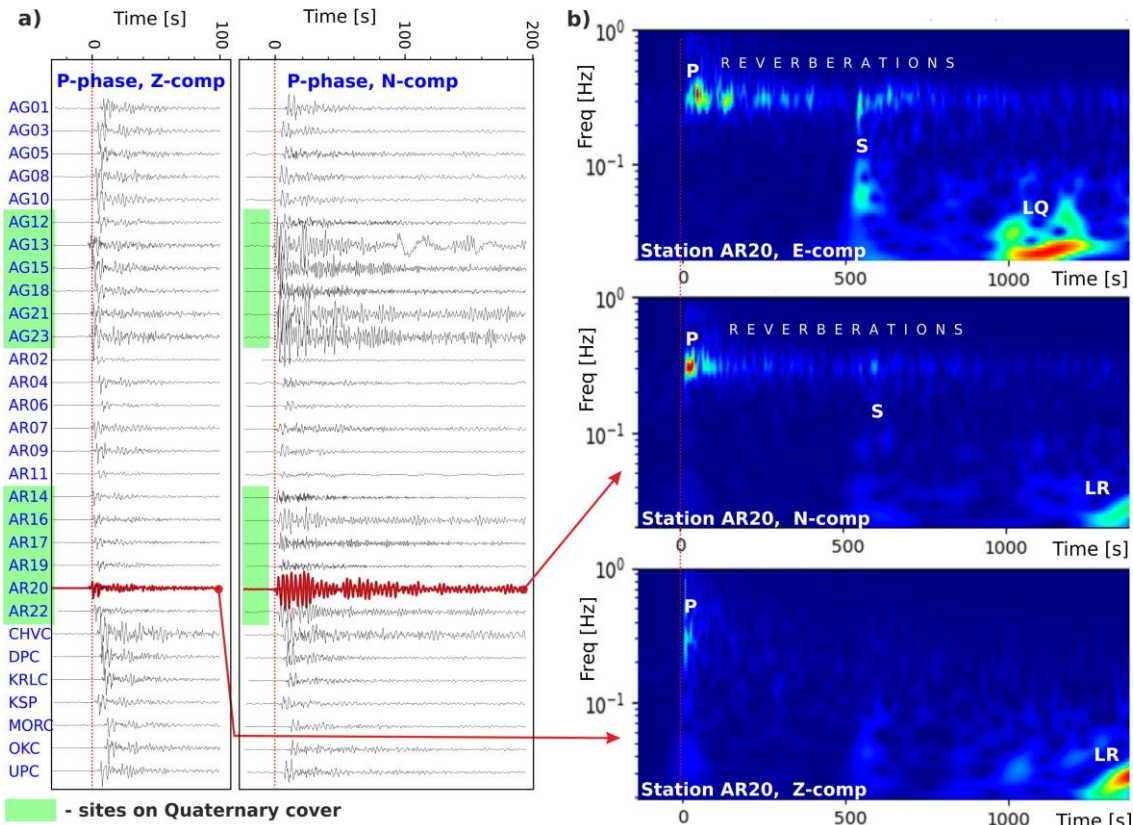
Figure 14: Seismic data example for event from 2018-11-30, 17:29:26 UTC, illustrating the differences in P-phase records between stations located on consolidated basement (short pulse, no reverberations) and sites located on young, unconsolidated cover (green rectangles, strong reverberations on the horizontal components). a) Z- and N-component records for all the stations used. b) ~~Spectral~~ 3-component spectral seismograms for station AG20. E- and N-components show high amplitude, > 600 s long coda (reverberations) in a narrow frequency range, centered at 0.3 Hz. The coda is non-existent in the Z-component record. True amplitude scaling was applied. Time scale is relative to theoretical P-phase onset.

The presence of the low-velocity sediments in the area of Sudetic Foreland is also related to another effect, affecting the character of the P-phase onsets. The P-wave pulses on the horizontal components are followed by a prominent, high-amplitude coda/reverberations, extending over up to several hundreds of seconds (Fig. 14). The coda is characterized by a narrow frequency range, with a central frequency of 0.25 - 0.40 Hz (periods of 2.5 - 4 s), depending on the station location. The corresponding P pulses on the vertical component are much shorter and seem to be only weakly affected (or not affected) by the coda. In contrast, for the stations located on the consolidated basement such reverberations are not observed on any component (Fig. 14a).

Such phenomenon is well known for a long time ~~was long recognized~~ and described by several authors, e.g. by Zelt and Ellis (1999) or Yu et al. (2015), as it may heavily distort the results of 3-component interpretation methods. A layer of low-velocity sediments, with a strong impedance contrast relative to the consolidated or crystalline basement, produces multiple

P-to-S conversions and reflections between the free surface and the base of the sediments. bottom. This results in high-amplitude reverberations in a narrow frequency range, mostly visible on the horizontal components. The frequency of the multiples is directly related to the seismic velocity and the thickness of the low-velocity layer. A systematic determination of the properties of the near-surface layer is out of scope of this paper. However, these observations can be compared with studies of the North Eastern part of the study area (LGCD), where the properties of the low-velocity layer were studied by Mendecki et al. (2016). They used the Horizontal to Vertical Spectral Ratio (HVSR) method to analyse the resonance frequencies and amplification factors based on the data collected by a broadband station in Tarnówek (Fig. 3), located ~15 km to the East of AR20 station. The HVSR peaks at 3.6–4.2 s were found, and Vs of ~0.4 km/s was estimated for a ~380 m thick CeCenozoic layer at this location. In our study, the Fig. 14b shows shorter (3.3 s) main period of the coda for AR20 station, which most likely correspond to thinningner of the sedimentary layer, or, higher S-wave velocity.

The reverberations related to a low-velocity layer pose significant problems for the interpretation of the data, e.g., with the receiver function technique, as they overprint Ps conversion pulses on the radial component. One of the methods to overcome this problem was presented by Yu et al. (2015). As the reverberations exhibit a resonant frequency related to the two-way traveltime of the wave in the sediment layer, the approach is based on designing a resonance removal filter in the frequency domain with filter parameters derived from the properties of the autocorrelation of the calculated RF. Our first tests showed that such filter, applied to the data from Sudetic Foreland, is quite effective and significantly reduces the effect of reverberations.

3.2 Verification of sensors misorientation

In the case of seismological methods which require three-component seismic recordings, such as receiver function analysis or shear-wave splitting method, precise sensor orientation is crucial to get correct results. Significant misorientation of the seismometers can adversely affect the reliability of final results and the interpretation. During the installation of stations in the field, to assure correct orientation, an azimuth measurement system with GNSS RTK unit and a MEMS gyroscope was used, as described in Sect. 2.3. According to our estimates, such system allows for determination of the N direction at the sensor location with ±2° accuracy, if appropriate care is taken by the operator during all steps of the procedure. In order to additionally check for possible misorientation of the sensors after deployment, using the acquired data, a method based on the analysis of the P-wave polarization described by Fontaine et al. (2009) was applied. These estimates were verified with the use ofusing a method proposed by Braunmiller et al. (2020), based on the P-wave polarization, and with approach of Doran and Laske (2017) based on polarization of the Rayleigh waves. The two latter methods are implemented in the OrientPy package (Audet, 2020).

Assuming a homogeneous and isotropic medium, in a seismogram recorded by For a correctly oriented sensor and a homogeneous, isotropic medium, the polarization of the P-wave and of the Rayleigh wave particle motion is expected to be confined to the ray plane, and its horizontal component to be polarized -parallel to the event backazimuth. The misorientation

of the seismometer (deviation of the N seismometer axis from the geographical North by *A* degrees - equivalent to rotation of the coordinate frame of the measurement system) will obviously result in an apparent deviation of polarization of the P-wave from the ray direction by an angle -*A*, independently of the event backazimuth. However, in real medium, this deviation can be superimposed by the effects of the heterogeneity (dipping velocity discontinuities) or anisotropy of the medium under the station. (Crampin et al., 1982; Schulte-Pelkum et al., 2001; Fontaine et al., 2009). These effects show a specific azimuthal dependence of resulting deviation angles (periodic with 180° or 360° period), therefore it is often possible to separate these factors, if data from a wide range of backazimuths are available. The total directional variability of the polarization deviation can be decomposed as (Schulte-Pelkum et al., 2001):

$$D_{pol}(\alpha) = A + B\sin(2\alpha) + C\cos(2\alpha) + D\sin(\alpha) + E\cos(\alpha) , \qquad (1)$$

where particular terms reflect the magnitude of various factors: A – the constant (azimuth-independent) component of polarization deviation, directly related to the incorrect sensor orientation; B and C – effect of anisotropy with horizontal symmetry axis; D and E – effect of anisotropy with inclined axis or effect of an inclined discontinuity; α – the event backazimuth.

For the analysis, from 165 events in the epicentral distance range of 5°-100°, the recordings with high signal-to-noise ratio on the vertical component of the P-phase (SNR > 5) were selected for each station. Selected data were filtered (various sub-bands of 2-16 s period band were used) and 3-D particle motion at the P-onset was analysed with the use of~~using~~ the orthogonal distance regression (ODR) method implemented in the ObsPy package, providing the azimuthal angle of the motion in the horizontal plane and incidence angle. Also, rectilinearity as defined by Fontaine et al. (2009) was calculated and was used to reject arrivals with poor rectilinearity of the particle motion, as contaminated by noise or other effects, and likely to produce distorted results. The error of the azimuthal angle was determined based on calculated eigenvalues of the particle motion (Fontaine et al., 2009). In order to improve stability of final results, individual D_{pol} values were sorted into backazimuthal bins of 30° width and averaged. Subsequently, these mean values were used for fitting the curve based on the equation (1) and for calculation of A-E parameters. The constant parameter A corresponds to the sensor misorientation.

To verify the results, we also analysed the same data set with a recently released software package OrientPy (Audet, 2020). The package implements two methods of determination of sensor orientation. The method described by Braunmiller et al. (2020) (BNG) determines the direction of P-wave polarization by minimizing the energy on the transverse component in a selected window around P-wave onset (Wang et al., 2016). Subsequently, polarizations for all events are averaged. The averaged value represents the constant component of the azimuth-dependent deviations, and is related to the misorientation angle for given station. It should be noted that the BNG method relies on relatively uniform backazimuthal coverage of the analysed data – averaging of a non-uniformly sampled sinusoidal curve is likely to result in a biased estimate of the mean value. Obtaining the mean value A by fitting the function~~curve~~ (1~~X~~) to the points as proposed by Fontaine et al. (2009) should produce more reliable result if the azimuthal distribution of the data is highly inhomogeneous.

475 The Doran and Laske (2017) method (DL) is based on Rayleigh-wave polarization analysis. For each event, a search is done for an angle α (defined relatively to theoretical backazimuth) which maximizes the cross-correlation between the Hilbert transform of the vertical component and the radial component rotated by α. As in the BNG method, calculated individual deviations for all the analysed events are averaged to get a value of the misorientation of individual stations.
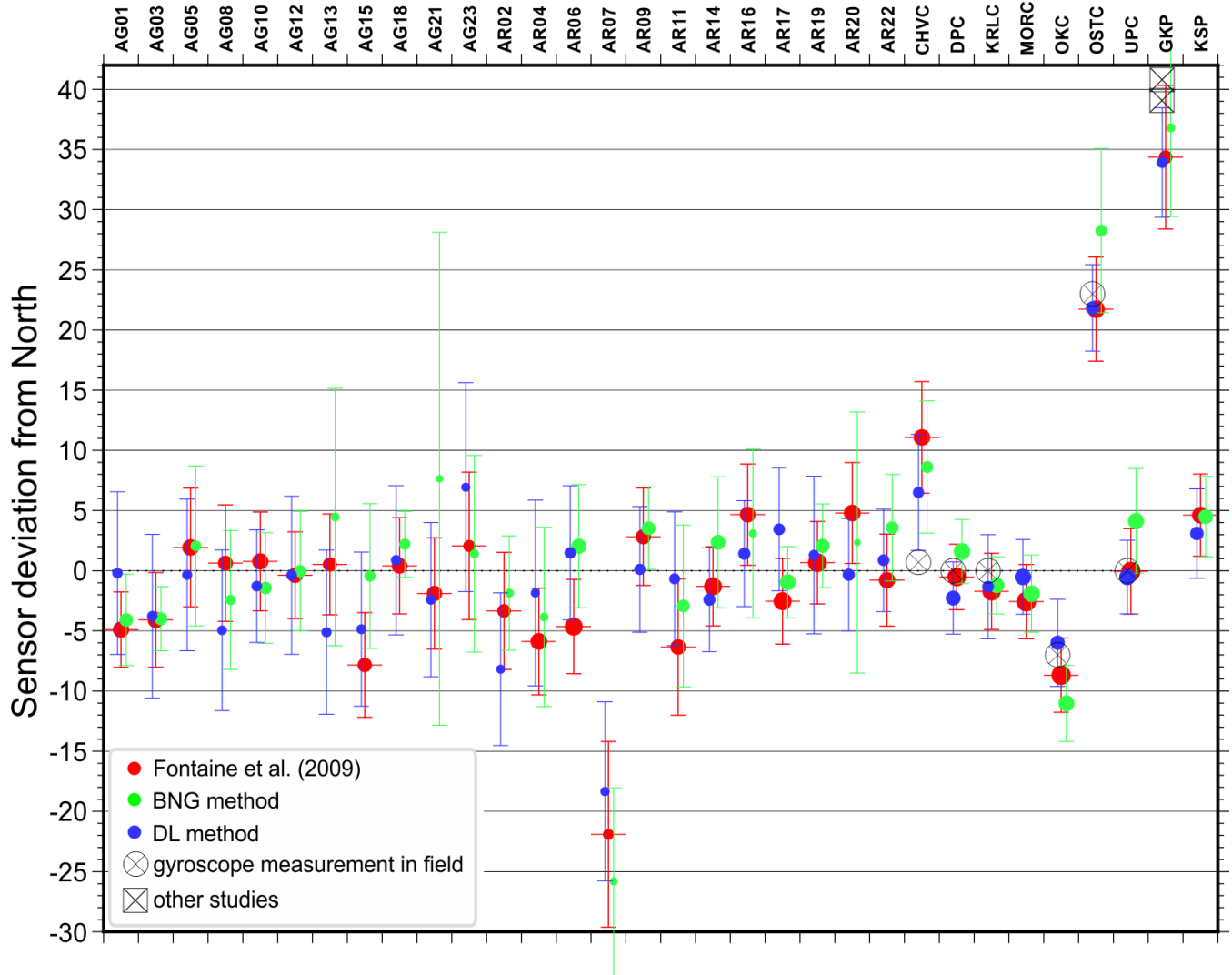
480 **Figure 15: Misorientation angles calculated for all stations using three described methods: red dots – Fontaine et al. (2009) method, green dots – BNG method, blue dots – DL method. Black circles with crosses – orientation angles of permanent stations from direct, high accuracy measurements~~measured using direct (gyroscope) methods~~ in field by gyrocompass (Vecsey L., Institute of Geophysics of Czech Academy of Sciences, personal communication, 2020). Black squares with crosses (for GKP station) – orientation angles reported by other studies (Vecsey et al., 2014; Wilde-Piórko et al., 2017).**

485

Figure 15 shows ~~obtained~~ values of misorientations of all stations in the study area obtained with the use of~~using~~ three described methods (the permanent station GKP is outside the study area, but it is shown for comparison, as previous studies also reported its significant misorientation - Vecsey et al. (2014) reported 41°, Wilde-Piórko et al. (2017) reported 39° and 45°, result of this study: 34-37°. ~~The measured sensor misorientation is significant for AR07, OSTC and GKP stations, with absolute values in a range of 20°-37°. For most other stations, the values do not exceed the range -7° to +7°.~~ For many stations, the results derived from the three methods are more or less consistent, but with some conspicuous exceptions. It can result from a small amount of recordings used for analysis because of low SNR for several stations.

For some permanent stations of the Czech Regional sSeism~~icological n~~Network (CHVC, DPC, KRLC, OKC, OSTC and UPC) the orientation angles obtained from direct, high accuracy gyrocompass measurements in field were available (Vecsey L., Institute of Geophysics of Czech Academy of Sciences, personal communication, 2020). They are presented as a reference in Fig. 15. For almost all these stations (except CHVC) our results are in a good agreement (in a ± 2-3° range) to the gyrocompass~~direct~~ measurements.

Table 2. Misorientation angles for all stations, obtained by~~from~~ different~~three~~ methods. Last column shows values from high-precision gyrocompass measurements or from other studies (if available), ~~and from direct measurements in field, if available. (*) not a direct measurement, result of Wilde-Piórko et al. (2017). (**) not a direct measurement, result of Vecsey at al., (2014).~~

Station code	Fontaine (2009) (°)	BNG method (°)	DL method (°)	other studies/ gyrocompass (°)
AG01	-4.9 ± 3.1	-4.1 ± 3.8	-0.2 ± 6.8	--
AG03	-4.1 ± 3.9	-4.0 ± 2.7	-3.8 ± 6.8	--
AG05	1.9 ± 4.9	2.1 ± 6.7	-0.4 ± 6.3	--
AG08	0.6 ± 4.8	-2.4+/-5.8	-5.0 ± 6.7	--
AG10	0.8 ± 4.1	-1.4 ± 4.6	-1.3 ± 4.7	--
AG12	-0.4 ± 3.6	-0.0 ± 5.0	-0.4 ± 6.6	--
AG13	0.5 ± 4.2	4.5 ± 10.7	-5.1 ± 6.8	--
AG15	-7.8 ± 4.4	-0.5 ± 6.0	-4.9 ± 6.4	--
AG18	0.4 ± 4.0	2.2 ± 2.7	0.9 ± 6.2	--
AG21	-1.9 ± 4.6	7.6 ± 20.5	-2.4 ± 6.4	--
AG23	2.1 ± 6.1	1.4 ± 8.2	6.9 ± 8.7	--
AR02	-3.3 ± 4.9	-1.9 ± 4.8	-8.2 ± 6.3	--
AR04	-5.9 ± 4.4	-3.9 ± 7.5	-1.9 ± 7.7	--
AR06	-4.6 ± 3.9	2.0 ± 5.1	1.5 ± 5.6	--
AR07	-21.9 ± 7.7	-25.8 ± 7.8	-18.3 ± 7.4	--
AR09	2.8 ± 4.1	3.5 ± 3.4	0.1 ± 5.2	--
AR11	-6.4 ± 5.7	-2.9 ± 6.7	-0.7 ± 5.6	--
AR14	-1.3 ± 3.3	2.4 ± 5.5	-2.4 ± 4.3	--
AR16	4.7 ± 4.2	3.1 ± 7.0	1.4 ± 4.4	--
AR17	-2.5 ± 3.6	-1.0 ± 3.0	3.4 ± 5.1	--
AR19	0.7 ± 3.4	2.1 ± 3.5	1.3 ± 6.6	--

AR20	4.8 ± 4.2	2.3 ± 10.9	-0.3 ± 4.7	--
AR22	-0.8 ± 3.8	3.6 ± 4.4	0.9 ± 4.3	--
KSP	4.6 ± 3.4	4.5 ± 3.3	3.1 ± 3.7	--
GKP	34.4 ± 6.0	36.8 ± 7.4	33.9 ± 4.6	41 (Vecsey et al., 2014) 39 ± 2 (Wilde-Piórko et al., 2017) 45 ± 4 (Wilde-Piórko et al., 2017)
CHVC	11.1 ± 4.6	8.6 ± 5.5	6.5 ± 4.8	0.7
DPC	-0.5 ± 2.7	1.6 ± 2.7	-2.3 ± 3.0	0.0
KRLC	-1.7 ± 3.2	-1.2 ± 2.4	-1.3 ± 4.3	0.0
MORC	-2.6 ± 3.1	-1.9 ± 3.2	-0.5 ± 3.1	--
OKC	-8.7 ± 3.1	-11.0 ± 3.2	-6.0 ± 3.6	-7.0
OSTC	21.7 ± 4.3	28.3 ± 6.8	21.8 ± 3.6	23.0
UPC	-0.1 ± 3.6	4.1 ± 4.4	-0.5 ± 3.1	0.0

Station Code	Fontaine (2009) method	BNG method	DL method	Direct measurement
AG01	-4.90 ± 3.14	-4.09 ± 3.80	-0.21 ± 6.76	--
AG03	-4.09 ± 3.94	-3.99 ± 2.66	-3.78 ± 6.80	--
AG05	1.93 ± 4.93	2.06 ± 6.65	-0.35 ± 6.30	--
AG08	0.63 ± 4.84	-2.43 +/- 5.77	-4.95 ± 6.67	--
AG10	0.78 ± 4.11	-1.44 ± 4.60	-1.28 ± 4.68	--
AG12	-0.38 ± 3.60	-0.04 ± 4.97	-0.38 ± 6.57	--
AG13	0.53 ± 4.19	4.45 ± 10.69	-5.11 ± 6.82	--
AG15	-7.83 ± 4.35	-0.45 ± 6.01	-4.86 ± 6.41	--
AG18	0.41 ± 4.01	2.20 ± 2.73	0.87 ± 6.20	--
AG21	-1.89 ± 4.63	7.64 ± 20.48	-2.41 ± 6.41	--
AG23	2.06 ± 6.13	1.41 ± 8.17	6.94 ± 8.68	--
AR02	-3.34 ± 4.86	-1.86 ± 4.76	-8.18 ± 6.34	--
AR04	-5.88 ± 4.43	-3.85 ± 7.45	-1.85 ± 7.72	--
AR06	-4.64 ± 3.91	2.04 ± 5.12	1.48 ± 5.57	--
AR07	-21.91 ± 7.72	-25.82 ± 7.77	-18.34 ± 7.44	--
AR09	2.82 ± 4.05	3.53 ± 3.42	0.11 ± 5.23	--
AR11	-6.35 ± 5.66	-2.93 ± 6.72	-0.67 ± 5.56	--
AR14	-1.30 ± 3.29	2.36 ± 5.45	-2.41 ± 4.32	--
AR16	4.66 ± 4.20	3.09 ± 7.02	1.42 ± 4.40	--
AR17	-2.54 ± 3.56	-0.96 ± 2.96	3.44 ± 5.11	--
AR19	0.66 ± 3.42	2.07 ± 3.47	1.30 ± 6.55	--
AR20	4.79 ± 4.19	2.34 ± 10.85	-0.34 ± 4.68	--
AR22	-0.78 ± 3.83	3.57 ± 4.43	0.87 ± 4.26	--
KSP	4.62 ± 3.42	4.49 ± 3.34	3.09 ± 3.72	--
GKP	34.36 ± 5.97	36.80 ± 7.37	33.92 ± 4.55	39 ± 2 (*), 45 ± 4 (*) 41 (**)

CHVC	11.07 ± 4.64	8.61 ± 5.50	6.50 ± 4.82	0.70
DPC	-0.52 ± 2.72	1.60 ± 2.66	-2.27 ± 3.00	0.00
KRLC	-1.72 ± 3.16	-1.22 ± 2.38	-1.33 ± 4.33	0.00
MORC	-2.57 ± 3.09	-1.91 ± 3.21	-0.52 ± 3.10	--
OKC	-8.68 ± 3.09	-11.03 ± 3.16	-5.99 ± 3.62	-7.00
OSTC	21.73 ± 4.33	28.26 ± 6.82	21.84 ± 3.59	23.00
UPC	-0.05 ± 3.55	4.13 ± 4.35	-0.53 ± 3.06	0.00

It must be noted that the results of the indirect, polarization-based, methods are not as precise as direct orientation measurements, e.g., with the optical gyrocompass. According to Rueda and Mezcua (2015), the Rayleigh wave polarization method achieves 1–5° uncertainty in case for long time spans of observations, e.g., at permanent stations, while for shorter time intervals the uncertainty can exceed 10°. Therefore, as pointed out by Vecsey et al. (2017), in case of temporary arrays with limited period of data acquisition, the methods based on polarization analysis are able to detect only substantial (> ~10°) misorientation of seismometers. Consequently, for our data, we decided that only results documenting misorientation above 10° were meaningful, and only for these stations seismograms will be corrected by an appropriate rotation. The values of the misorientation calculated by three methods for all the stations are summarized in the Table 2.

For most of the stations, the orientation values obtained from polarization analysis agree, within the error bounds, with the orientations measured directly at the sites with GPS/gyroscope system, as can be seen in the Figure 15 and in the Table 2 (the estimated error bounds for both methods are ~ ±3-7° (largely) and ±2°, respectively). Therefore, we assume that the orientation of these stations determined by GPS/gyroscope can be considered as correct (0° misorientation). However, for five other stations, the polarization analysis results differ significantly from the orientations measured at the sites - AR07, OSTC and GKP (absolute orientation values of ~ 20°-37°), CHVC and OKC (~9°), suggesting that these sensors were incorrectly oriented during installation. The seismograms from these stations need to be rotated to a correct NE coordinate frame before use, and orientation codes in the headers of original (unrotated) data need to be set to Z, 1 and 2 instead of Z, N and E, according to the Standard for the Exchange of Earthquake Data (SEED) definition.

4 Conclusions and perspective

The AniMaLS project is an experimental seismic study of the physical properties and geological structure of the lithosphere and sub-lithospheric mantle beneath the Polish Sudetes (NE margin of the Variscan orogen), with a complex history of tectonic evolution. The acquisition of the seismic data involved deployment of 23 broadband stations for the period of ~ 2about two years (Oct 2017 – Oct 2019). The selection of sites and installation was done using a low-cost approach, with the stations deployed inside the unused basements, sheds or in rarely used public utility buildings. The stations were powered through the power grid, and the data were collected with the use ofusing near real-time data transmission over the UMTS network. During the measurement period, over 97% of data were retrieved. Location of the sites in the vicinity of the

inhabited areas increased the safety, the ease of installation and the reliability of the data transmission, however, at the cost of the noise level, which was higher compared to the permanent stations in the region. Overall, the installed network~~array~~ provided a reliable acquisition of the continuous, partly broadband seismic data ~~of good quality~~ in near real-time. The acquired records of local, regional and teleseismic events will be used as data for various seismic interpretation methods in order to determine velocity distribution, anisotropy and location of discontinuities in the upper mantle. ~~.~~

~~Analysis of P receiver functions will allow for imaging of the lithospheric discontinuities, in particular of the Moho boundary, and for comparison of the obtained Moho depths with the results from the wide-angle data modelling, e.g., from the SUDETES 2003 seismic experiment (Grad et al., 2003) or based on other active seismic studies. Also, deeper mantle (410 km and 660 km) discontinuities will be imaged. Based on the S receiver functions and on the analysis of surface waves, a study of the lithosphere asthenosphere boundary depth and properties will be attempted. The upper mantle anisotropy will be studied using shear wave splitting analysis, based on the recordings of the SKS and SKKS phases. The analysis of the P-wave polarization may also contribute to anisotropy studies. The research on the anisotropy and its variations can provide the information on the direction and degree of frozen in lithospheric deformations or on the asthenospheric mantle flow, as well as on the petrological characteristics of the mantle. The mantle studies will benefit from a good knowledge of the crustal structure beneath the Sudetes, obtained based on previous active source experiments and geological information from drillings.~~

~~In the past, the study area was covered by a single Polish seismic station KSP only, therefore the newly obtained recordings of the local events, acquired by the AniMaLS array, can be also of a great help for studies of the local seismicity, seismotectonics and in seismic hazard assessment.~~

Obtained geophysical results will be integrated with ~~other geophysical and~~ geological research, as, ~~data~~ e.g., ~~For instance, recent results of the petrological~~ studies of anisotropy of the mantle xenoliths from the Sudetes. ~~in the Tertiary volcanics (Puziewicz et al., 2012), abundant in Sudetes, will be used to complement the seismic results and to help to interpret the origins of the mantle anisotropy.~~ A multidisciplinary synthesis involving the results of the seismic interpretation can serve as a basis for inferences about relative movements of the tectonic units forming the area, about the impact of orogenic and other deformational events on the present structure, and can help to reconstruct the history of geological evolution of the NE Variscan orogen and of the neighboring areas.

Data availability: ~~D~~The data from the AniMaLS experiment are stored at the IG PAS (https://dataportal.igf.edu.pl/dataset/animals), currently with restricted access (https://doi.org/10.25171/InstGeoph_PAS_IGData_AniMaLS_2021_002). The dataset will be open for the scientific community three years from the completion of the database, i.e., in 2023.

Supplement: The Supplement related to this article is available online at…

Author contributions: Article preparation was done by MB and PŚ with contributions from all co-authors. MB participated in data acquisition, QC, processing and PPSD analysis. JR participated in data acquisition, QC, processing and analysis of stations misorientation. DW designed the azimuth-transfer system and participated in data acquisition. WM participated in data acquisition, QC and processing. PŚ designed the experiment, directed and participated in data acquisition, QC, processing and analyses.

Team list: The AniMaLS Working Group comprises: Marek Grad[1,†], Tomasz Janik[2], Kuan-Yu Ke[2,3], Marcin Polkowski[1] and Monika Wilde-Piórko[1,4].

1 Faculty of Physics, Institute of Geophysics, University of Warsaw, Warszawa, 02-093, Poland

2 Department of Seismic Lithospheric Research, Institute of Geophysics Polish Academy of Sciences, Warszawa, 01-452, Poland

3 Helmholtz Centre Potsdam, GFZ German Research Centre for Geosciences, Telegrafenberg, 14473, Potsdam, Germany

4 Institute of Geodesy and Cartography, Warszawa, 02-679, Poland

† deceased

Competing interests: The authors declare that they have no conflict of interests.

Acknowledgements

The project was funded by the National Science Center (grant no. UMO-2016/23/B/ST10/03204). Some of the figures were created with Generic Mapping Tool software (Wessel and Smith, 1995). We thank people participating in preparation and deployment of the seismic stations: T. Arant, M. Chmielewski, E. Gaczyński, J. Grzyb, S. Oryński, T. Skrzynik, J. Suchcicki. Special thanks for Jan Wiszniowski for numerous valuable advices. We are grateful to the reviewers: Simon C. Stähler, Wolfram Geissler and the anonymous reviewer for their constructive comments, which helped us to improve the manuscript.

References

Aleksandrowski, P., Kryza, R., Mazur, S., and Żaba, J.: Kinematic data on major Variscan strike-slip faults and shear zones in the Polish Sudetes, northeast Bohemian Massif, Geological Magazine, 133, 727–739, 1997.

Audet, P.: OrientPy: Seismic station orientation tools (Version v0.0.1), Zenodo, DOI: 10.5281/zenodo.3905404, 2020.

Beyreuther, M., Barsch, R., Krischer, L., Megies, T., Behr, Y., and Wassermann, J.: ObsPy: A Python Toolbox for Seismology, Seismological Research Letters, 81 (3), 530-533, doi: 10.1785/gssrl.81.3.530, 2010.

Babuška, V., Plomerová, J., and Vecsey, L.: Mantle fabric of western Bohemian Massif (central Europe) constrained by 3D seismic P and S anisotropy, Tectonophysics, 462, 149–163, DOI: 10.1016/j.tecto.2008.01.020, 2008.

595 Braunmiller, J., Nabelek, J., and Ghods, A.: Sensor Orientation of Iranian Broadband Seismic Stations from P-Wave Particle Motion, Seismological Research Letters, 91 (3), 1660-1671, 2020.

Crampin, S., Stephen, R. A., and McGonigle, R.: The polarization of P-waves in anisotropic media, Geophysical Journal International, 68 (2), 477-485, 1982.

Custódio, S., Dias, N. A., Caldeira, B., Carrilho, F., Carvalho, S., Corela, C., Díaz, J., Narciso, J., Madureira, G., Matias, L.,
600 Haberland, C., and WILAS Team: Ambient Noise Recorded by a Dense Broadband SeismicDeployment in Western Iberia, Bulletin of the Seismological Society of America, 104(6), 2985-3007, 2014.

Daubechies, I.: Ten Lectures on Wavelets, SIAM, Philadelphia, PA, USA, p. 357, 1992.

Doran, A. K. and Laske, G.: Ocean-bottom seismometer instrument orientations via automated Rayleigh-wave arrival-angle measurements, Bulletin of the Seismological Society of America, 107(2), 691-708, 2017.

605 Ekström, G. and Busby, R. W.: Measurements of Seismometer Orientation at USArray Transportable Array and Backbone Stations, Seismological Research Letters, 79 (4), 554-561, 2008.

Evangelidis, C. P. and Melis, N. S.: Ambient Noise Levels in Greece as Recorded at the Hellenic Unified Seismic Network, Bulletin of the Seismological Society of America, 102 (6), 2507-2517, 2012.

Fontaine, F. R., Barruol, G., Kennett, B. L., Bokelmann, G. H., and Reymond, D.: Upper mantle anisotropy beneath
610 Australia and Tahiti from P wave polarization: Implications for real-time earthquake location, Journal of Geophysical Research: Solid Earth, 114 (B3), 2009.

Franke, W., Cocks, L. R. M., and Torsvik, T. H.: The Palaeozoic Variscan oceans revisited, Gondwana Research, 48, 257-284, DOI: 10.1016/j.gr.2017.03.005, 2017.

Geological map 1 : 50000 [online]. Praha: Czech Geological Survey [2021-01-11]. Available from:
615 https://mapy.geology.cz/geocr50

Geissler, W.H., Kämpf, H., Skácelová, Z., Plomerová, J., Babuška, V., and Kind, R.: Lithosphere structure of the NE Bohemian Massif (Sudetes) — A teleseismic receiver function study, Tectonophysics, 564–565, 12–37, DOI: 10.1016/j.tecto.2012.05.005, 2012.

Grad, M., Guterch, A., Mazur, S., Keller, G.R., Špičák, A., Hrubcová, P., and Geissler, W. H.: Lithospheric structure of the
620 Bohemian Massif and adjacent Variscan belt in central Europe based on profile S01 from the SUDETES 2003 experiment, Journal of Geophysical Research, 113, B10304, DOI: 10.1029/2007JB005497, 2008.

Grad, M., Špičàk, A., Keller, G. R., Guterch, A., Brož, M., Hegedüs, E., and Working Group: SUDETES 2003 Seismic Experiment, Studia Geophysica et Geodaetica, 47(3), 681-689, DOI: 10.1023/A:1024732206210, 2003.

ISC Bulletin, available from: http://www.isc.ac.uk/iscbulletin (last access: December 2020), 2020.

625 Kind, R., Handy, M.R., Yuan, X., Meier, T., Kämpf, H., and Soomro, R.: Detection of a new sub-lithospheric discontinuity in central Europe with S receiver functions, Tectonophysics, 700, 19-31, DOI:10.1016/j.tecto.2017.02.002, 2017.

Krischer, L., Megies, T., Barsch, R., Beyreuther, M., Lecocq, T., Caudron, C., and Wassermann, J.: ObsPy: a bridge for seismology into the scientific Python ecosystem, Computational Science & Discovery, 8(1), 014003, DOI:10.1088/1749-4699/8/1/014003, 2015.

630 Knapmeyer-Endrun, B., Krüger, F., Legendre, C.P., Geissler, W.H., and PASSEQ Working Group: Tracing the influence of the Trans-European Suture Zone into the mantle transition zone, Earth and Planetary Science Letters, 363, 73–87, 2013.

Majdański, M., Grad, M., Guterch, A., and SUDETES 2003 Working Group: 2-D seismic tomographic and ray tracing modelling of the crustal structure across the Sudetes Mountains basing on SUDETES 2003 experiment data, Tectonophysics, 413, 249-269, 2006.

635 Mazur, S., Aleksandrowski, P., Gągała, Ł., Krzywiec, P., Żaba, J., Gaidzik, K., and Sikora, R.: Late Palaeozoic strike-slip tectonics versus oroclinal bending at the SW outskirts of Baltica: case of the Variscan belt's eastern end in Poland, International Journal of Earth Sciences, 1-28, 2020.

Mazur, S., Aleksandrowski, P., Turniak, K., and Awdankiewicz, M.: Geology, tectonic evolution and Late Palaeozoic magmatism of Sudetes — an overview, In: Kozłowski, A., and Wiszniewska, J. (eds.), Granitoids in Poland, AM Monograph
640 No. 1, Faculty of Geology of the Warsaw University, Warszawa, 59–87, 2007.

McNamara, D. and Buland, R. P.: Ambient Noise Levels in the Continental United States, Bulletin of the Seismological Society of America, 94(4),1517-1527, DOI: 10.1785/012003001, 2004.

Mendecki, M. J., Bieta, B., Mateuszów, M., and Suszka, P.: Comparison of site effect values obained by HVSR and HVSRN methods for single-station measurements in Tarnówek, South-Western Poland, Contemp. Trends. Geosci., 5(1), 18-27
645 DOI:10.1515/ctg-2016-0002, 2016.

Mirek, J. and Rudziński, Ł.: LUMINEOS-nowoczesna sieć sejsmologiczna do monitorowania sejsmiczności i poziomu drgań gruntu na obszarze eksploatacji złóż miedzi w Legnicko-Głogowskim Okręgu Miedziowym, Zeszyty Naukowe Instytutu Gospodarki Surowcami Mineralnymi Polskiej Akademii Nauk, 163-172, 2017.

Państwowy Instytut Geologiczny - Państwowy Instytut Badawczy, 2021. Mapa geologiczna Polski 1:500000, available from:
650 https://geologia.pgi.gov.pl (last access: 2021-01-11).

Peterson, J.: Observations and modeling of seismic background noise, U.S. Geol. Survey Open-File Report 93-322, 95 pp, 1993.

Plomerová, J., Vecsey, L., and Babuška, V.: Mapping seismic anisotropy of the lithospheric mantle beneath the northern and eastern Bohemian Massif (central Europe), Tectonophysics, 564–565, 38–53, DOI: 10.1016/j.tecto.2011.08.011, 2012.

655 Polkowski, M.: Lokalizacja ognisk trzęsień ziemi metodą propagacji wstecznej z wykorzystaniem implementacji metody fast marching w modelu 3D obszaru Polski, Doctoral dissertation, Institute of Geophysics, Faculty of Physics, University of Warsaw, 2016.

Puziewicz, J., Matusiak-Małek, M., Ntaflos, T., Grégoire, M., Kukuła, A.: Subcontinental lithospheric mantle beneath Central Europe, International Journal of Earth Sciences, 104, 1913–1924, 2015.

660 ~~Puziewicz, J., Czechowski, L., Krysiński, L., Majorowicz, J., Matusiak-Małek, M., and Wróblewska, M.: Lithospheric thermal structure at the eastern margin of the Bohemian Massif: a case petrological and geophysical study of the Niedźwiedź amphibolite massif (SW Poland), International Journal of Earth Sciences, 101, 1211-1228, 2012.~~

Rueda, J. and Mezcua, J.: Orientation Analysis of the Spanish Broadband National Network Using Rayleigh-Wave Polarization, Seismological Research Letters, 86(3), 929-940, 2015.

665 Růžek, B., Hrubcová, P., Novotný, M., Špičák, A., and Karousová, O.: Inversion of travel times obtained during active seismic refraction experiments CELEBRATION 2000, ALP 2002 and SUDETES 2003, Studia Geophysica et Geodaetica, 51, 141–164, 2007.

Ryczywolski, M., Oruba, A., and Leończyk, M.: The precise satellite positioning system ASG-EUPOS, International Conference GEOS 2008 Proceedings, 27-28.02.2009, Prague (Czech Republic), VUGTK, Praha 2008.

670 Schulte-Pelkum, V., Masters, G., and Shearer P. M.: Upper mantle anisotropy from long-period P polarization, Journal of Geophysical Research: Solid Earth, 106 (B10), 21917-21934, 2001.

Sens-Schönfelder, C.: Synchronizing seismic networks with ambient noise, Geophysical Journal International, 174, 3, 966-970, 2008.

Stähler, S.C., Schmidt-Aursch, M.C., Hein, G., Mars, R.: A Self-noise model for the German DEPAS OBS pool, Seismolog-
675 ical Research Letters, 89 (5), 1838–1845. DOI: 10.1785/0220180056, 2018.

~~Staehler, S. C., Sigloch, K., Hosseini, K., Crawford, W. C., Barruol, G., Schmidt-Aursch, M. C., Tsekhmistrenko, M., Scholz, J. R., Mazzullo, A., and Deen, M.: Performance report of the RHUM-RUM ocean bottom seismometer network around La Reunion, western Indian Ocean, Advances in Geosciences, 41, 43-63, DOI: 10.5194/adgeo-41-43-2016, 2016.~~

Tanimoto, T., Yano, T., and Hakamata, T.: An approach to improve Rayleigh-wave ellipticity estimates from seismic noise:
680 application to the Los Angeles Basin, Geophysical Journal International, 193, 407-420, 2013.

Tasič, I. and Runovc, F.: Seismometer self-noise estimation using a single reference instrument, Journal of Seismology, 16(2), 183–194, DOI: 10.1007/s10950-011-9257-4, 2012.

Tilmann, F.: Recording of local earthquakes in Simeulue, NERC Geophysical Equipment Facility, Scientific Report 800, 2006.

685 U. S. Geological Survey: GTOPO30, DOI: 10.5066/F7DF6PQS, 1996.

Vecsey, L., Plomerová, J., and Babuška, V.: Mantle lithosphere transition from the East European Craton to the Variscan Bohemian Massif imaged by shear-wave splitting, Solid Earth, 5, 779-792, DOI: 10.5194/se-5-779-2014, 2014.

Vecsey, L., Plomerová, J., Jedlička, P., Munzarová, H., Babuška, V., and the AlpArray working group: Data quality control and tools in passive seismic experiments exemplified on the Czech broadband seismic pool MOBNET in the AlpArray
690 collaborative project, Geoscientific Instrumentation Methods and Data Systems Discussions, 6(2), 1-27, DOI: 10.5194/gi-6-505-2017, 2017.

Wang, X., Chen, Q. F., Li, J., and Wei, S.: Seismic sensor misorientation measurement using P-wave particle motion: An application to the NECsaids Array, Seismological Research Letters, 87 (4), 901-911, 2016.

Wessel, P. and Smith, W. H. F.: New version of Generic Mapping Tools released, EOS, 76, 453, 1996.

695 Wilde-Piórko, M., Geissler, W. H., Plomerová, J., Grad, M., Babuška, V., Brückl, E., Cyziene, J., Czuba, W., England, R., Gaczyński, E., Gazdova, R., Gregersen, S., Guterch, A., Hanka, W., Hegedüs, E., Heuer, B., Jedlička, P., Lazauskiene, J., Randy Keller, G., Kind, R., Klinge, K., Kolinsky, P., Komminaho, K., Kozlovskaya, E., Krüger, F., Larsen, T., Majdański, M., Málek, J., Motuza, G., Novotný, O., Pietrasiak, R., Plenefisch, T., Růžek, B., Sliaupa, S., Środa, P., Świeczak, M., Tiira, T., Voss, P., and Wiejacz, P.: PASSEQ 2006-2008: passive seismic experiment in Trans-European Suture Zone, Studia
700 Geophysica et Geodaetica, 52, 439–448, 2008.

Wilde-Piórko, M., Grad, M., and the POLONAISE working group: Regional and teleseismic events recorded across the TESZ during POLONAISE'97, Tectonophysics, 314, 161–174, 1999.

Wilde-Piórko, M., Grycuk, M., Polkowski, M., and Grad, M.: On the rotation of teleseismic seismograms based on the receiver function technique, Journal of Seismology, 21, 857-868, 2017.

705 Wilson, D., Leon, J., Aster, R., Ni, J., Schlue, J., Grand, S., Semken, S., Baldridge, S., and Gao, W.: Broadband seismic background noise at temporary seismic stations observed on a regional scale in the Southwestern United States, Bulletin of the Seismological Society of America, 92 (8), 3335-3341, 2002.

Yu, Y., Song, J., Liu, K. H., and Gao, S. S.: Determining crustal structure beneath seismic stations overlying a low-velocity sedimentary layer using receiver functions, J. geophys. Res.: Solid Earth, 20, 3208–3218, 2015.

710 Zelt, B. C. and Ellis, R. M.: Receiver-function studies in the Trans-Hudson Orogen, Saskatchewan, Can. J. Earth Sci., 603, 585–603, 1999.